Fiber Cavity Optomechanics with Polymer Membranes

Lukas Tenbrake

Masterarbeit in Physik
angefertigt am Institut für Angewandte Physik

vorgelegt der

Mathematisch-Naturwissenschaftlichen Fakultät

der

Rheinischen Friedrich-Wilhelms-Universität Bonn

October 2021

I hereby declare that the work presented here was formulated by myself and that no sources or tools other than those cited were used.

Bonn, 10.10.2021 .... Lukas Tenbrake ....

date signature

1. Gutachter: Prof. Dr. Dieter Meschede
2. Gutachter: Prof. Dr. Sebastian Hofferberth

Acknowledgments

First of all, I would like to thank Prof. Dr. Meschede for giving me the opportunity to work on such a fascinating project in his research group and also Prof. Dr. Hofferberth for being the second appraiser.

Moreover, I also have to thank the complete Quantum-Technologies group of Prof. Dr. Meschede for their help and advice, the Nanophotonik team of Prof. Dr. Linden for their collaboration and the Nonlinear Quantum Optics group of Prof. Dr. Hofferberth for welcoming me into their team.

Special thanks go to Alexander Faßbender from the Linden group for dealing with our numerous laser writing requests and Moritz Scharfstädt from the Köhl group for introducing me to the fiber shooting setup.

Furthermore, I would like to thank Carlos Saavedra for his help in getting me started in the lab and for being my lab partner for most of my thesis and also Dr. Hannes Pfeifer for his guidance during my master thesis, his always helpful advice and for sharing his vast knowledge about optomechanics.

At last, I would like to give thanks to the proofreaders of this thesis, Dr. Hannes Pfeifer, Richard Winkelmann and Roberto Valdivia.

Contents

Chapter 1

Introduction

The field of cavity optomechanics explores the interaction between mechanical motion and electromagnetic radiation in optical resonators. Historically, cavity optomechanics originated as a "by-product" of the developments in optical gravitational wave detectors in the late 1970s and has since flourished into an expansive field governing the classical and quantum mechanical interaction between optics and mechanics in devices from the microscopic- ($m \sim 10^{-20}$ g) to the macroscopic ($m \sim$ kg) scale [1]. Nowadays, optomechanical devices offer many potential applications ranging from extremely sensitive optical sensors of small forces [2] to unitary frequency converters between the optical- and microwave regime for quantum networking & computing [3].

Braginsky *et al.* demonstrated cavity optomechanical effects with microwaves [4] in pioneering experiments as early as 1967 and Dorsel *et al.* (1983) were the first to demonstrate radiation-pressure induced optomechanical interaction in a Fabry-Perot resonator with one suspended end-mirror [5]. These early developments spearheaded the discovery of many phenomena unique to optomechanics such as the optical spring effect [6], optomechanical dampening (leading to cooling of the mechanical resonator) [7] and optical bistability [5] displayed in a variety of novel cavity optomechanics systems ranging from nanorods inside Fabry-Perot cavities [8], photonic crystals [9], whispering gallery microdisks [10], cold atom clouds [11] and of course in its simplest realization a Fabry-Perot resonator with a suspended mirror. Very similar to the last device is the so-called "Membrane-in-the-Middle" (MIM) cavity (demonstrated in 2008 by [12]) again consisting of a Fabry-Perot cavity with two fixed mirrors and pliable (dielectric) membrane in-between. The major advantage of this system is the decoupling of optics and mechanics which allows for individual optimization without compromise between the two constituents. As reaching the quantum regime demands high performance of both optical and mechanical resonator [13], the MIM system offers a favorable platform for these purposes.

As our research group already successfully utilizes fiber-based Fabry-Perot micro-resonators ([14], [15]) for a wide range of applications, the choice for the optical constituent for the optomechanical experiments is obvious: Fiber-mirrors offer miniature size and small cavity mode volume while also offering simple interfacing due to the fiber-coupling [16], making it the ideal choice for the integration into more complex systems. Many established MIM experiments utilize commercial silicone nitride (SiN) membranes because of their high optical and mechanical quality [17]. These membranes then need to be integrated into the cavity, often increasing the size and complexity of the experimental setup. As a more compact and

lightweight approach, 3D laser written polymer structures can be directly integrated into the MIM cavity offering a flexible alternative to the SiN membranes. This flexibility, combined with the ease of interfacing such a system through fiber-coupling and its scaling capabilities to larger more complex systems makes it a promising platform for upcoming challenges in cavity optomechanics like versatile optomechanical sensor platforms, realization of multimode optomechanical experiments, investigation of quantum many-body physics in optomechanical arrays and many more.
Since our research group did not have an established experimental realization of such systems, the goal of this thesis was to show a proof of principle operation of this novel MIM platform to quantify its performance.
The first two chapters of this thesis are dedicated to the constituents of the MIM system and serve as an introduction and overview of their properties. The final chapter describes how the optical and mechanical mode couple, quantifies the expected coupling strength and finally presents the characterization measurements of the optomechanical system.

Chapter 2

Optics: Fiber Fabry-Perot cavities for optomechanical interaction

Compared to their free-space coupled counterpart, a fiber-based cavity system offers many advantages when it comes to the ease of in-coupling light into the resonator, while also offering a miniaturized and compact design. On the other hand, the small mode volumes V_{mode} provided by fiber resonators are useful for cavity QED experiments where the coupling between the intra-cavity field and atomic ensembles scale as $V_{\text{mode}}^{-1/2}$. For optomechanical applications, these cavities offer a great platform to integrate optomechanical components into resonator systems on a microscopic scale.

2.1 The Fabry-Perot cavity

In the following section, the core concepts of free-space coupled optical resonators are introduced. The longitudinal- and transversal modes of light inside the Fabry-Perot cavity are briefly explained and an introduction to the resonator stability criterion is given. The following section deals with the physics unique to Fiber-Fabry-Perot-Cavities (FFPC).

2.1.1 Basics of Fabry-Perot cavities

Since optical resonators are essential for performing cavity optomechanics, fundamental concepts and characteristics of the Fabry-Perot cavity (FPC) are reviewed briefly. A more in-depth analysis and derivation of the core results can be found in standard optics textbooks such as [18].

FPC: longitudinal modes In its simplest realization, a Fabry-Perot cavity consists of two highly reflective planar mirror surfaces (M_1 & M_2) each entirely described by their respective reflectivity (r_i), transmission (t_i) and losses (l_i) [1]. This configuration allows in-coupled light $\boldsymbol{\mathcal{E}}_{\text{in}}$ to be reflected back and forth a considerable amount of times (compare Fig. 2.1 (a)). If the light wave reproduces itself after one complete round trip, constructive interference of the partial fields builds up a strong intra-cavity field $\boldsymbol{\mathcal{E}}_{\text{circ}}$:

[1] The corresponding amplitudes $\mathcal{T}_i$, $\mathcal{R}_i$ and $\mathcal{L}_i$ are related as $\mathcal{R}_i = |r_i|^2 = 1 - \mathcal{T}_i - \mathcal{L}_i$

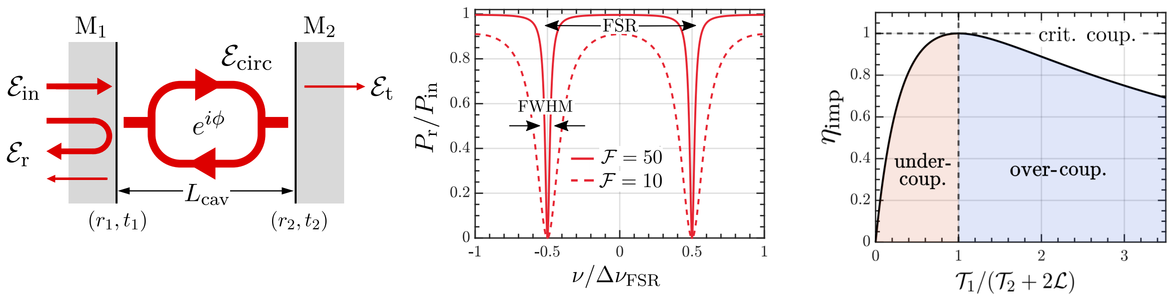

(a) (b) (c)

Figure 2.1: **(a)** Diagrammatic representation of the field distributions for a FPC with planar mirrors M$_1$ & M$_2$ separated by the cavity length $L_{\rm cav}$. **(b)** Normalized reflection spectrum (compare Eq. (2.3)) featuring two adjacent resonance dips with $\mathcal{F} = 10$ (dashed line) and $\mathcal{F} = 50$ (solid line). **(c)** Impedance-matching factor $\eta_{\rm imp}$ plotted against the loss ratio $\mathcal{T}_1/(\mathcal{T}_2 + 2\mathcal{L})$. A cavity is called over-(under-) coupled if $\mathcal{T}_1 > \mathcal{T}_2 + 2\mathcal{L}$ ($\mathcal{T}_1 < \mathcal{T}_2 + 2\mathcal{L}$), marked in the diagram as the blue (red) shaded area. For most applications it is preferred to maintain a critically coupled cavity, where $\mathcal{T}_1 = \mathcal{T}_2 + 2\mathcal{L}$.

$$\mathcal{E}_{\rm circ} = t_1 \mathcal{E}_{\rm in} \left(1 + r_1 r_2 e^{i\phi} + (r_1 r_2)^2 e^{2i\phi} + \dots\right) = \mathcal{E}_{\rm in} \frac{t_1}{1 - r_1 r_2\, e^{i\phi}} \tag{2.1}$$

where the additional phase shift due to reflection at the mirrors has been absorbed into the overall acquired phase shift $e^{i\phi}$ after one complete round-trip. In frequency space, the resulting power spectrum consists of an infinite collection of resonant longitudinal modes separated by the so-called Free-Spectral-Range (FSR) $\Delta\nu_{\rm FSR}$.

This (resonance) condition can be mathematically expressed by demanding that the phase of the light field $\phi = k \cdot 2L'_{\rm cav}$ must equal 2π after one round trip inside the cavity of length $L_{\rm cav}$ [2]. In total, this leads to a restriction on the frequency as $\nu = N \cdot \Delta\nu_{\rm FSR}$ where N is an integer.

Since the intra cavity field $\mathcal{E}_{\rm circ}$ is much less experimentally accessible, it is often common to probe the reflected (transmitted) spectrum $|\mathcal{E}_r|^2$ ($|\mathcal{E}_t|^2$). Realizing that the reflected field $\mathcal{E}_{\rm r}$ is just the sum of the immediately reflected input field $r_1\mathcal{E}_{\rm in}$ and the leakage of the build-up intrinsic field $\mathcal{E}_{\rm circ}$ and making use of Eq. (2.1), it follows that:

$$\mathcal{E}_{\rm r} = r_1 \mathcal{E}_{\rm in} - r_2 t_1 \mathcal{E}_{\rm circ}\, e^{i\phi} = \mathcal{E}_{\rm in} \left(\frac{r_1 - r_2(1-\mathcal{L}) e^{i\phi}}{1 - r_1 r_2\, e^{i\phi}} \right). \tag{2.2}$$

where the additional minus sign in front of $r_2 t_1 \mathcal{E}_{\rm circ}\, e^{i\phi}$ is due to one less reflection compared to the circulating field $\mathcal{E}_{\rm circ}$. The resulting periodic reflection spectrum, as shown in Fig. 2.1 (b), can be written as:

$$P_{\rm r} = P_{\rm in} \left(\frac{1 - \eta_{\rm imp} + (1-\mathcal{L}) \cdot 4\frac{\mathcal{F}^2}{\pi^2} \sin^2(\pi \frac{\nu}{\Delta\nu_{\rm FSR}})}{1 + 4\frac{\mathcal{F}^2}{\pi^2} \sin^2(\pi \frac{\nu}{\Delta\nu_{\rm FSR}})} \right) \tag{2.3}$$

under the assumption that $\mathcal{L}_1 = \mathcal{L}_2$ & $\mathcal{T}, \mathcal{L} \ll 1$. The factor $\mathcal{F} = 2\pi/\sum_i \mathcal{L}_i = 2\pi/(\mathcal{T}_1 + \mathcal{T}_2 + 2\mathcal{L})$ is the so-called Finesse of the cavity. It characterizes the optical quality

[2] here, $L'_{\rm cav}$ corresponds to the optical length of the cavity defined by $L'_{\rm cav} = n \cdot L_{\rm cav}$, where n is the refractive index of the medium between mirrors M$_1$ & M$_2$ and $L_{\rm cav}$ their geometric separation. For the sake of visual clarity, the dash will be suppressed.

of the resonator and is proportional to the enhancement of the injected power $\mathcal{T}_1 P_{\text{in}}$ for the circulating field $\mathcal{E}_{\text{circ}}$. It furthermore links two important frequency measures of the reflected spectrum in the FSR and the Full-Width-Half-Maximum (FWHM) $\Delta\nu_{\text{FWHM}}$ via $\mathcal{F} = \Delta\nu_{\text{FSR}}/\Delta\nu_{\text{FWHM}}$.

η_{imp} is the so-called impedance-matching factor and determines how well the injected power is coupled to the cavity system. Mathematically, it can be expressed as:

$$\eta_{\text{imp}} = 1 - \left(\frac{\mathcal{T}_2 - \mathcal{T}_1 + 2\mathcal{L}}{\mathcal{T}_2 + \mathcal{T}_1 + 2\mathcal{L}} \right)^2 \tag{2.4}$$

If the overall losses $(\mathcal{T}_2 + 2\mathcal{L})$ exactly equal the input transmission amplitude $\mathcal{T}_1$, the two fields from Eq. (2.2) interfere destructively which results in no reflected power on resonance. This type of cavity configuration is called critically coupled whereas for an over-(under-) coupled cavity the overall losses are smaller (greater) than the input transmission amplitude and feature reflected powers on resonance ($P_r = (1 - \eta_{\text{imp}})\, P_{\text{in}}$) greater than zero (compare 2.1 (c)).

FPC: Transversal modes Light coupled into a resonator that exhibits a steady transverse intensity profile that does not change after successive reflections off the mirrors is called a (transversal) (TEM_{nm} [3]) mode of the cavity. This condition implies that the wavefront of the resonator mode features the same radius of curvature as the one at each mirror end, making the light wave retrace its original path [19]. With this in mind, the situation inside a resonator is, therefore, to first-order, entirely described by the geometry of the cavity: the radii of curvature R_i of the mirrors and their separation L_{cav} (compare Fig. 2.2 (a)).

The lowest order mode that features the simplest spatial distribution and has the most practical application is the so-called fundamental mode (TEM_{00}). Its intensity profile features a decaying radially symmetric pattern that can be expressed as:

$$I(r, z) = I_0 \left(\frac{\omega_0}{\omega(z)} \right)^2 \exp\left(-2r^2/\omega^2(z) \right) \sin^2(kz). \tag{2.5}$$

It features a tightly focused waist $2\,\omega_0$ from which the beam diverges outwards along the cavity axis (here z-axis) described by $\omega(z)$. The $\sin^2(kz)$ takes account for the standing wave (longitudinal mode) that is present within a stable resonator. Typical Gaussian beam parameters are summarized in Tab. 2.1.

2.1.2 Resonator stability and alignment

For most applications, the TEM_{00} mode is the most desirable mode to operate a cavity at. It features the smallest beam waist, the least amount of beam divergence and a transversal intensity pattern without nodes [20]. Assuming the input laser beam with laser power P_{in} operates at the aforementioned fundamental mode, a perfectly aligned cavity would solely host this particular input mode, i.e all higher-order TEM_{nm} modes would not be supported by the resonator. In this case one talks about a so-called mode-matched cavity, meaning that the overlap between the input mode and cavity mode is at maximum (quantified by the mode-matching factor ϵ).

[3] Transversal Electromagnetic Mode. The indices n and m correspond to the amount of nodes present in the transverse intensity profile, see Fig. 2.2 (b) and (c).

Formular Table for Gaussian Beams

bare intensity	$I_0 = \frac{c\epsilon_0}{2}\|E_0\|^2$	(2.6)
beam radius	$\omega(z) = \omega_0\sqrt{1+\left(\frac{z}{z_\mathrm{R}}\right)^2}$	(2.7)
Rayleigh length	$z_\mathrm{R} = \pi\omega_0^2/\lambda$	(2.8)
beam waist size	$\omega_0 = \left(\frac{\lambda L_\mathrm{cav}}{\pi}\right)^{\frac{1}{2}}\left[\frac{g_1 g_2(1-g_1 g_2)}{(g_1+g_2-2g_1 g_2)^2}\right]^{\frac{1}{4}}$	(2.9)
g-parameters	$g_i = 1 - \frac{L_\mathrm{cav}}{R_i}$	(2.10)

Table 2.1: Formular Table displaying typical Gaussian beam parameters. For the radii of curvature, the convention $R_i < 0$ for concave and $R_i > 0$ for convex mirrors is used.

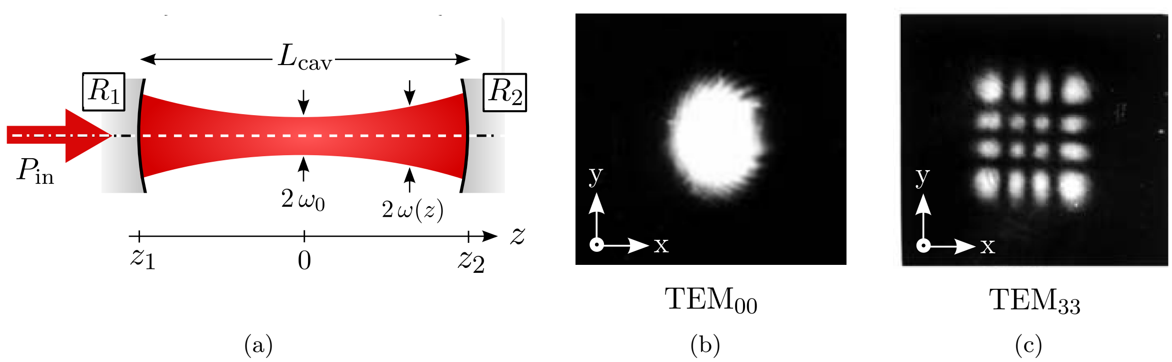

Figure 2.2: **(a)** Geometry of the fundamental TEM$_{00}$ mode. The cavity field is confined by two opposing mirrors at position z_1 with radius of curvature R_1 and z_2 with R_2 respectively. The diameter of the Gaussian intensity profile diverges from the beam waist $2\omega_0$ to a value of $2\,\omega(z)$ at position z. **(b)** and **(c)** Transverse intensity profile of the TEM$_{00}$ and TEM$_{33}$ mode, featuring zero nodes and three vertical and horizontal nodes, respectively. Images adapted from [19].

In reality, this overlap will most often not be maximized due to an overall misalignment of the cavity geometry. This can reveal itself in many different forms (besides the more apparent tilt and transversal offset between the mirror geometry itself), to name a few: transverse displacement and tilt of the laser input axis with respect to the cavity axis, beam waist size mismatch and longitudinal waist displacement. A sketch featuring these different scenarios is displayed in Fig. 2.3 (a).

When misaligned, higher-order TEM$_\mathrm{nm}$ modes will also couple to the cavity and will exhibit, depending on the mirror geometry, non-degenerate resonance frequencies besides the wanted fundamental frequency [21]. To combat this, mode-matching optics (e.g lense systems) can be employed to reduce these effects. For rigid [4] single-mode fiber cavities (see section 4.4), the magnitude of the misalignment will be determined by the quality of the fiber mirror

[4] A rigid fiber cavity contains the two opposing fiber mirrors in a bore of a glass ferrule, eliminating the need to geometrically align the cavities.

fabrication. Since the options to improve the alignment post-production are limited, careful consideration must be given to reduce fabrication-based flaws in the fiber mirror geometry.

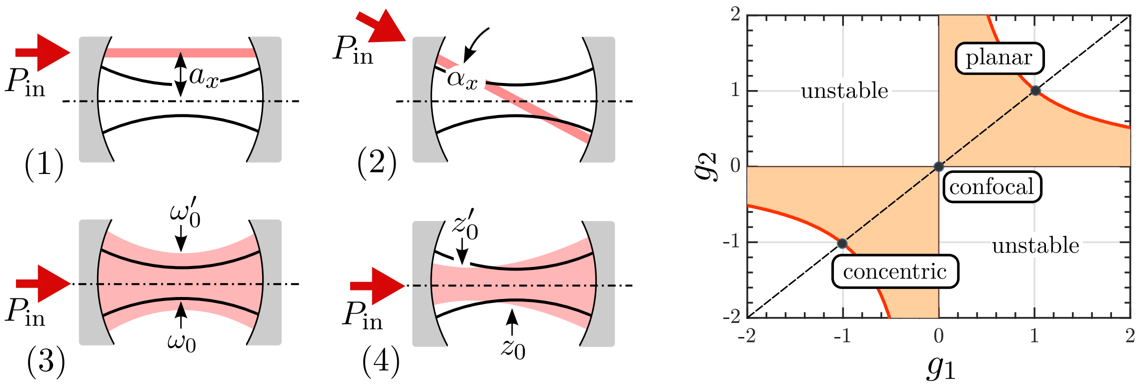

(a) (b)

Figure 2.3: **(a)** Diagrammatic sketch of the field inside a cavity for 4 exemplary cases of misalignment. The cavity mode for optimal alignment is outlined in black: **(1)** Transverse displacement a_x between the input laser beam and resonator. **(2)** Tilt angle α_x between input laser beam and resonator. **(3)** Mismatched beam waist between resonator (ω_0) and input laser beam (ω_0'). **(4)** Mismatched beam waist position between resonator (z_0) and input laser beam (z_0'). **(b)** Stability diagram of an optical resonator. The yellow shaded area describes all resonator configuration abiding by the stability criterion $0 \leq g_1 g_2 \leq 1$. Three special (symmectric) cases are highlighted: the planar cavity ($R_1 = R_2 = \infty$), the confocal cavity ($R_1 = R_2 = L_{\text{cav}}$) and the concentric cavity ($R_1 = R_2 = L_{\text{cav}}/2$).

A further aspect to consider is the stability of a resonator: not all arbitrary combinations of mirror geometries will form a stable cavity. A resonator is considered stable if after an appreciable amount of reflections the light beam stays inside the resonator. If this is not the case, the resonator is said to be unstable. In a more concrete fashion, one can define a stability criterion in terms of the g-parameters (see Tab. 2.1) which demands that the Rayleigh length z_R (see Tab. 2.1), the distance along the propagation direction from the waist to the position where the area of the cross-section is doubled, must be a real number. This results in the so-called stability criterion for spherical [5] mirrors:

$$0 \leq g_1 g_2 \leq 1 \tag{2.11}$$

With this, a stability diagram (compare Fig. 2.3 (b)) can be plotted which shows the regions in which stable optical resonators can be built. It displays the edge cases for cavities that are just on the outskirts of the stable region, and are therefore very prone to becoming unstable with only slight misalignment. In this thesis, the most common types of resonators employed will be the "semi-hemispherical" resonator consisting of one concave and one flat mirror with both mirrors showing much larger radii of curvature R_i compared to the cavity length L_{cav}. Further details on the specific cavity geometry parameters that were chosen can be seen in section 2.4.

[5] A flat mirror is considered to be a spherical mirror with infinite radius of curvature.

2.2 Physics of fiber Fabry-Perot cavities

In this section, a brief overview of the most relevant physical attributes of fiber Fabry-Perot cavities (FFPC) is presented. The asymmetric reflection line shape associated with fiber-based cavities is quantified by employing the "Bra-Ket" notation known from standard quantum mechanics literature [22] to introduce spatial overlaps of optical modes in a compact fashion. In analog to section 2.1.2, the optical mode-matching factor ϵ will be introduced to describe the effects of (fiber) cavity misalignment on the optical coupling of the cavity.

2.2.1 Coupling to fiber Fabry-Perot cavities

To keep the notation compact and short, the electric fields E_i at hand will be separated into two components: firstly, the complex amplitude of the field and its corresponding phase factors $\mathcal{E}_i$ and secondly, the transversal mode profile $|\psi_i\rangle$ containing the spatial-distribution information. This leads to a compact way to write down an arbitrary electric field E_i as:

$$E_i = \mathcal{E}_i \cdot |\psi_i\rangle$$

The (normalized) transversal mode distributions follow the Dirac "Bra-Ket" notation with an accompanying inner product $\langle \psi \mid \phi \rangle$ defined as

$$\begin{aligned} \langle \psi \mid \phi \rangle &= \int_{-\infty}^{+\infty} \int_{-\infty}^{+\infty} \psi^*(x,y)\phi(x,y) dx dy \\ &= \int_{-\infty}^{+\infty} \psi_x^*(x)\phi_x(x) dx \int_{-\infty}^{+\infty} \psi_y^*(y)\phi_y(y) dy \end{aligned} \tag{2.12}$$

which is recognized as the spatial overlap between two optical modes. Since all of the transversal modes are considered to be fundamental Gaussian modes, the overlap integral can thus be split up into two one dimensional integrals over the respective (x, y)-plane — at coordinate z_0 — perpendicular to the propagation axis z (see Eq. 2.12). It is therefore sufficient to only consider one spatial direction (from this point on just the x-coordinate) to understand the physics of fiber-mirror cavities.

To calculate the reflective line shape of a fiber cavity (in analogue to section 2.1.1 in free-space coupled cavities), the individual contributions to the electric fields involved in the cavity field are named as follows: the directly reflected field from the mirror on the in-coupling side $|\psi_r\rangle$, the forward (+) and backward (−) propagating guided fiber mode $\left|\psi_{\mathrm{f}}^{\pm}\right\rangle$ and the intra-cavity mode $\left|\psi_{\mathrm{cav}}^{\pm}\right\rangle$. The mode-matching factor ϵ that determines how efficient the in-coupling mode couples to the intra-cavity mode is given by [23]:

$$\epsilon = \left| \left\langle \psi_{\mathrm{cav}}^{+} \mid \psi_f^{+} \right\rangle \right|^2 \tag{2.13}$$

For free-space coupled cavities, the overall in-coupling efficiency is given by the relative alignment of the cavity mirrors and the guiding of the in-coupling laser propagating into the cavity. Assuming that, in the case for fibers, the mirrors are fixed (e.g inside a ferrule) and the in-coupling of the laser beam is not further altered (e.g. by GRIN [6] - fiber assemblies [24]), the mode matching factor ϵ is determined by the geometry of the spherical mirror that

[6] **Gr**aded-**In**dex (GRIN)

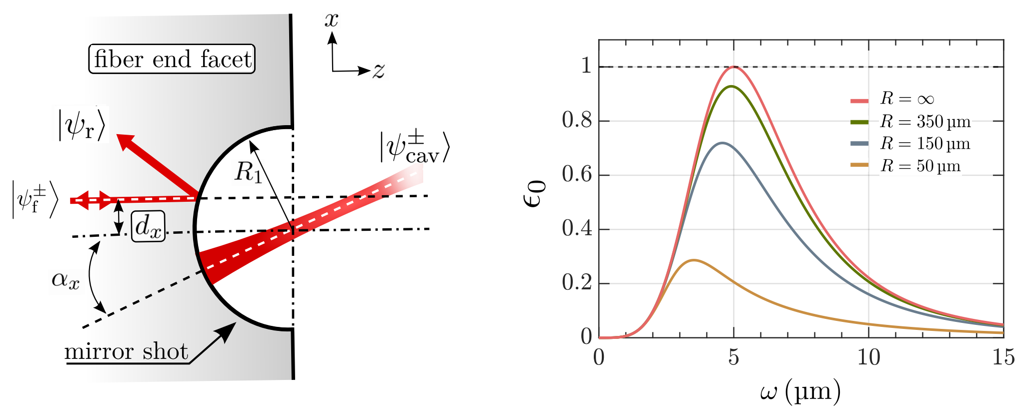

(a) (b)

Figure 2.4: **(a)** Cross-section of the fiber end facet in the x-z-plane for the geometrical and optical considerations for approximating the mode-matching coefficient ϵ. To simplify, the fiber mirror geometry is to be assumed as a perfect circular shape. The fiber mirror displayed here features two common forms of fiber misalignments: a decentered fiber mirror compared to the fiber core (quantified by d_x) and a tilt of the intra-cavity mode (quantified by α_x). **(b)** Mode-matching coefficient ϵ_0 for different mirror radii of curvature with an exemplary fixed fiber mode radius $\omega_f = 5\,\mu\mathrm{m}$.

is shot onto the fiber end facet (see Fig. 2.4 (a)). In a simplified model assuming fundamental Gaussian modes, the mode matching factor epsilon ϵ of a perfectly aligned and centered cavity is given by [25]:

$$\epsilon_0 = \frac{4}{\left(\frac{w_{\mathrm{f}}^2}{w^2} + \frac{w^2}{w_{\mathrm{f}}^2}\right)^2 + \left(\frac{k w_{\mathrm{f}} w}{2R}\right)^2} \tag{2.14}$$

with the fiber mode radius ω_f, Gaussian beam radius ω (for a particular z-point), wave vector k and mirror radius of curvature R. A diagram displaying the optical mode matching coefficient ϵ_0 for a fixed fiber mode waist ω_f and different mirror radii of curvature R is shown in Fig. 2.4 (b).

If one now includes potential misalignment either via a decentered mirror shot (compare Fig. 2.4 (a)), mirror cleave angle [7], a tilted fiber mirror or the two fiber-mirrors not being vertically aligned and centered with respect to each other, the total mode matching factor (considering both x- and y-directions) from Eq. 2.14 is modified to:

$$\epsilon = \epsilon_0 e^{-2d^2/d_e^2} e^{-2\alpha^2/\alpha_e^2}$$

with effective length d_e and angle α_e depending on the geometry of the cavity [23]. With this, a cavity is said to be perfectly mode matched if there are no geometric and optical misalignments, the beam waist of the in-coupling fiber mode and cavity perfectly match and the wavefront curvature is sufficiently large compared to the beam waist of the system.

[7] For the fabrication of fiber-mirrors, a straight clean fiber-end-facet is required. A potential slant from the cutting/cleaving-process will also introduce misalignment that will hurt the overall coupling-efficiency.

2.2.2 Reflection line shape of fiber Fabry-Perot cavities

As touched upon in section 2.1.1, the free-space coupled cavity features a symmetric reflection line shape that — close to resonance — can be approximated by a Lorentzian line shape, where the (coupling) depth of the line shape on resonance is given by $P_{\text{CD}} = \epsilon \cdot \eta_{\text{imp}} \cdot P_{\text{in}}$. For a fiber-based cavity system, the major difference arises from the additional mode filtering that takes place inside the fiber core: as in the free-space case, the total reflected field that will be measured consists of the immediately reflected part of the input power E_r given by:

$$E_r = r_1 \cdot \mathcal{E}_{\text{in}} \left|\psi_r\right\rangle \simeq \mathcal{E}_{\text{in}} \left|\psi_r\right\rangle \tag{2.15}$$

interfering with the leakage from the intra-cavity field (compare Fig. 2.5)

$$\begin{aligned} E_{\text{leak}}(\Delta v) &= -t_1 \cdot \mathcal{E}_{\text{circ}} \cdot r_2 e^{i\phi} \left|\psi_{\text{cav}}^-\right\rangle \\ &= -\mathcal{E}_{\text{in}} \frac{t_1^2 r_2 e^{i\phi}}{1 - r_1 r_2 e^{i\phi}} \left\langle \psi_{\text{cav}}^+ \mid \psi_f^+ \right\rangle \left|\psi_{\text{cav}}^-\right\rangle \end{aligned} \tag{2.16}$$

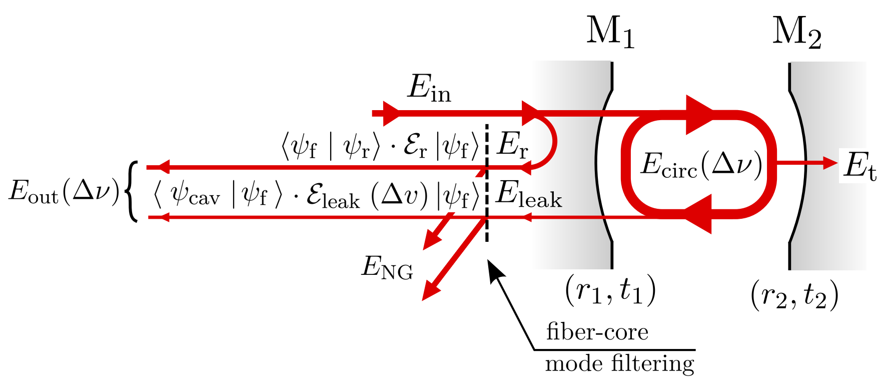

Figure 2.5: Schematic representation of the light-coupling procedure within a fiber-mirror cavity. The back-reflected field E_{NG} that is filtered out of the fiber core is lost and scattered into the surrounding fiber cladding. The total output field $E_{\text{out}}(\Delta\nu)$ is thus given by the interference between the immediately reflected field E_r and the cavity leakage field E_{leak}. A small part of the field E_t is also transmitted through the second fiber mirror.

where $\mathcal{E}_{\text{circ}}$ is the intra-cavity electric field amplitude introduced in section 2.1.1, $\phi = 2\pi\Delta\nu/\Delta\nu_{\text{FSR}}$ the round trip-phase with detuning $\Delta\nu$ from the cavity resonance frequency and additional mode overlap $\left\langle \psi_{\text{cav}}^+ \mid \psi_f^+ \right\rangle$ between fiber and intra-cavity mode.

Both parts are propagating through the fiber mirror core back to the measurement apparatus, but only the spatial mode that overlaps with the fiber-core mode can be efficiently coupled and guided back into the fiber, the residue is therefore filtered out into the surrounding fiber-cladding (see Fig. 2.5). With this, the light that is guided back into the fiber core reads:

$$\begin{aligned} E_{\text{out}}(\Delta\nu) &= \left(\left\langle \psi_f^- \right| E_r + \left\langle \psi_f^- \right| E_{\text{leak}}(\Delta v)\right) \mid \psi_f^- \rangle. \\ &= \mathcal{E}_{\text{in}} \left(\left\langle \psi_f^- \mid \psi_r \right\rangle - \frac{t_1^2 r_2 e^{i\phi}}{1 - r_1 r_2 e^{i\phi}} \left\langle \psi_{\text{cav}}^+ \mid \psi_f^+ \right\rangle \left\langle \psi_f^- \mid \psi_{\text{cav}}^- \right\rangle\right) \left|\psi_f^-\right\rangle. \end{aligned} \tag{2.17}$$

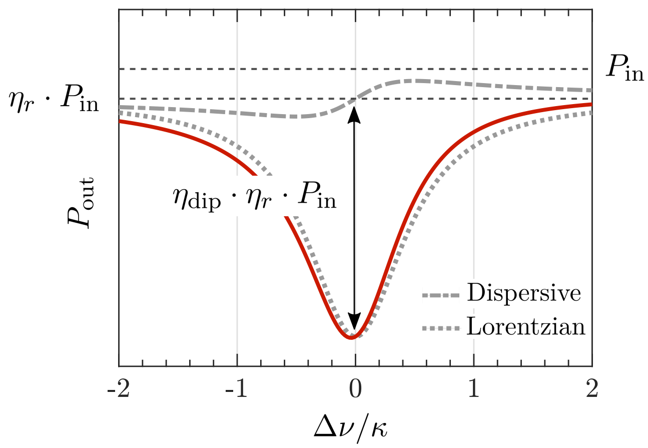

Figure 2.6: Illustration of the contributions to the overall reflection line shape (red) of a fiber cavity. The overall reflected power is reduced by the mode-filtering factor η_r with on-resonance coupling depth $P_{\text{CD}} = \eta_{\text{dip}} \cdot \eta_r \cdot P_{\text{in}} = \epsilon \cdot \eta_{\text{imp}} \cdot \eta_r \cdot P_{\text{in}}$.

The reflected power can thus be Taylor-expanded ($\Delta\nu \ll \Delta\nu_{\text{FSR}}$) to:

$$\frac{P_{\text{out}}(\nu)}{P_{\text{in}}} = \left|\frac{E_{\text{out}}(\nu)}{E_{\text{in}}}\right|^2 = \eta_r - \eta_{\mathscr{L}} \left(\frac{1}{1+\nu^2} - \mathscr{A}\frac{\nu}{1+\nu^2}\right) \tag{2.18}$$

with the normalized detuning $\nu = \Delta\nu/\kappa$ where $\kappa = \Delta\nu_{\text{FWHM}}/2$ is the so-called cavity decay rate. The resulting line shape (see Fig. 2.6) of the reflected power is a combination of a symmetric Lorentzian lineshape with amplitude $\eta_{\mathscr{L}}$ and asymmetric dispersive lineshape with overall amplitude $\eta_{\mathcal{L}} \cdot \mathcal{A}$, which depend on the overlap integrals $\langle \psi_f^- \mid \psi_r \rangle$ and $\langle \psi_{\text{cav}}^+ \mid \psi_f^+ \rangle$ (for further details, refer to [25]). The reflection baseline of the fiber cavity is reduced by a factor $\eta_r = \left|\langle \psi_f^- \mid \psi_r \rangle\right|^2$ compared to the free-space coupled resonator, which describes the mode-overlap of the immediate reflected input field with the back-propagating fiber-core mode.

2.2.3 Additional effects to consider

Clipping losses As touched upon in section 2.1.1, the Finesse of a resonator with mirrors M_i, $i = 1, 2$ is given by the inverse of the sum of all losses associated with the resonator. More specifically, these typically consist of intrinsic scattering $L_{\text{scat,i}}$, absorption $L_{\text{abs,i}}$ and transmission losses T_i of the reflective coating on the fiber-end facet. They are coating-specific losses that can be found in any Bragg-mirror-based cavity and are not unique to fiber cavities. An additional loss channel that is especially relevant for FFPCs however, is the so-called clipping loss L_{clip} and can be estimated to [16]:

$$\mathcal{L}_{\text{clip,i}} = \exp\left(-\frac{D_{\text{i}}^2}{4w_{\text{i}}^2}\right). \tag{2.19}$$

If the size of the beam radius ω_i of the cavity mode at the fiber mirror end facets is comparable to the mirror diameter D_i itself, an appreciable amount of light will not be reflected back into the resonator but instead will be clipped due to the finite mirror diameter size. This leads to the updated Finesse formula:

$$\mathcal{F} = \frac{2\pi}{\sum_{i=1,2}\left(\mathcal{L}_{\mathrm{abs,i}} + \mathcal{L}_{\mathrm{scat,i}} + \mathcal{L}_{\mathrm{clip,i}} + T_{\mathrm{i}}\right)}. \tag{2.20}$$

With this addition, the Finesse of a fiber-based cavity will now depend on the chosen cavity length L_{cav} and can not be arbitrarily selected without consequence. It is therefore important to always choose a cavity length below the clipping threshold to ensure that no clipping of the cavity light mode takes place. For the cavities utilized here, clipping losses generally start to take place above $L_{\mathrm{cav}} \approx 50\,\mu\mathrm{m}$ but are not of major concern for the typical cavity lengths of $L_{\mathrm{cav}} = 20 - 30\,\mu\mathrm{m}$ employed in this thesis.

Polarization-mode splitting Polarization-mode splitting lifts the degeneracy between the orthogonal linear-polarization modes inside the cavity, leading to a frequency splitting Δv_{spl} of their resonance frequencies [26]:

$$\frac{\Delta v_{\mathrm{spl}}}{\Delta v_{\mathrm{FWHM}}} = \frac{\mathcal{F}}{2\pi}\Delta\varphi \tag{2.21}$$

with the differential phase-shift $\Delta\phi$ between the two orthogonal modes. Next to stress-induced birefringence in the mirror coatings, fabrication-flaws in the fiber mirror geometry (e.g elliptical mirrors) are the largest contributor to polarization-mode splitting in fiber-based cavities. Additional corrections to the paraxial resonator theory [27] show that the resonance frequency of a linearly polarized cavity mode depends on the mirror's radius of curvature along the polarization direction. Ellipticity in the laser-machined fiber mirrors would therefore introduce an unwanted splitting of the cavity resonance.
However, since the cavities used in thesis are all operating in the low Finesse regime (above GHz linewidths), the effect of the mode splitting (MHz) on the cavity resonance (for decently well-fabricated fiber mirrors) is minimal and can be safely neglected.

2.3 Fiber mirror fabrication

This section will give a very brief introduction to the laser ablation process for carving spherical mirrors into fiber-end facets used in our in-house fiber fabrication facility. Furthermore, a brief description of how said mirrors are implemented into the experiment is given. As the fabrication of laser-machined fiber mirrors is not the main focus of this work, only a very brief introduction suffice for the context of this thesis is given. For a more in-depth exploration, refer to one of the many theses dedicated to our in-house fiber mirror fabrication (e.g [24], [28]).

To fabricate spherical micro-depressions on cleaved fiber-end facets, a high-power CO_2 laser operating at $\lambda = 9.3\,\mu\mathrm{m}$ is employed. Since the laser wavelength lies within the absorption peak of fused Silica (SiO_2) [29], the optical power of the laser can be transformed into heat which effectively evaporates the illuminated portion of the fiber-end facet. To efficiently ablate surfaces into suitable micro-mirror structures, low surface roughness and ellipticity are required, which can be achieved by applying radially symmetric Gaussian beam pulses to the surface. After the shooting process, a thin layer of molten silica remains and smoothens the surface of the fiber as it solidifies. In the end, a Gaussian-like depression profile is left on the

surface of the fiber, which acts as an approximately spherical mirror depression [8] close to the origin of the shot, with typical radii of curvature of $R \approx 150 - 250\,\mu\mathrm{m}$.
After the ablation process, the shot fibers are then sent to a coating company [9] that deposit alternating dielectric layers of Ta_2O_5 ($n = 2.10$) and SiO_2 ($n = 1.45$) (each with a thickness of $\lambda/4$) to create Bragg-mirrors. With this, reflectivities of up to 99.99% over a frequency range of approximately $770 - 820\,\mathrm{nm}$ can be achieved. To now make the shot and coated fiber mirrors usable for the experiments, a commercial fusion splicer machine [10] is used to fuse the fiber mirror to a commercial single-mode fiber patch cable with build-in fiber-couplers that allow for simple integration into optical setups.
For this, a few centimeters of the fiber-end opposite to the mirror are inserted into a $FeCl_3$ solution for 15 minutes, stripping off the outer protective copper coating of the fiber and exposing the bare cladding layer. A manual fiber cleaver [11] is used to cut a straight end facet of the bare fiber, needed to ensure minimal optical losses in the spliced interface (typically around 0.2 dB after a successful splice). The same cleaving procedure is then performed on half of a commercial single-mode fiber patch cable, after which both fiber ends can be properly spliced together.

2.4 Hybrid fiber Fabry-Perot cavities

This section details how the fiber mirrors are actually utilized in the experiments and the corresponding measurement techniques employed to infer information about the cavity. The setup is based on a hybrid cavity consisting of an in-coupling fiber mirror that couples light into the resonator opposing a macroscopic 0.5 inch flat mirror. The latter will later host the different 3D laser written polymer structures for the optomechanics experiments, but for now, is just assumed to be bare. Information about the cavity is extracted using a standard reflection-based measurement technique explained in the following. As this setup plays a crucial role for all of the following experiments in this thesis, a more general overview of the system is given ignoring the optomechanical context for now.
The hybrid cavity setup and the corresponding reflection-based measurement scheme are depicted in Fig. 2.7 (a). A wavelength-tunable laser [12] set to $\lambda = 780\,\mathrm{nm}$ with roughly 20 mW output power is guided through a Polarizing-Beam-Splitter (PBS) into the fiber-coupler input of the spliced fiber mirror (refer to section 2.3). Waveplates are set up before and after the PBS and are adjusted in a way that any back-reflected light experiences a 90° rotation in the polarization and exits the PBS on the port that leads to a photodiode. Most of the light that is coupled into the single-mode fiber mirror (transmission $T_1 = 2000\,\mathrm{ppm}$ and curvature $R \approx 150\,\mu\mathrm{m}$) is promptly reflected back towards the photodiode. If, however, the cavity length L_{cav} is equal to $\lambda/2$ a resonance occurs and the back-reflected light destructively interferes with the field that is leaking out of the cavity (compare section 2.2).

The power (voltage) measured on the photodiode would reduce given by the coupling depth of the cavity, and in the ideal case, go down to zero. Since it is difficult to modify the cavity

[8] This is the best-case scenario. Any factors that "pollute" the laser-beam profile — e.g effects such as astigmatism — may lead to unwanted mirror ellipticity [25].
[9] Laseroptik GmbH: https://www.laseroptik.com/
[10] Ericsson FSU PM
[11] Fitel S-324 Fiber Cleaver
[12] Lion Series: TEC-500-0770-040

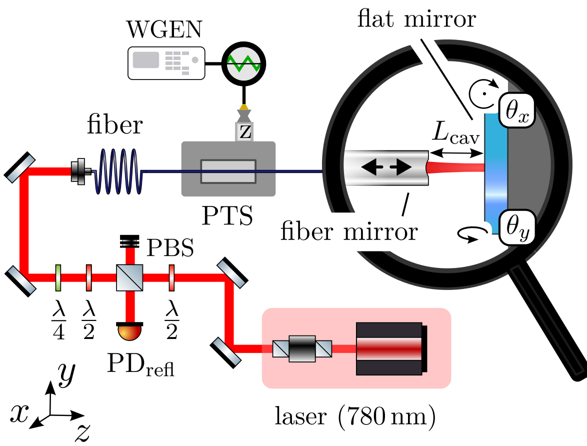

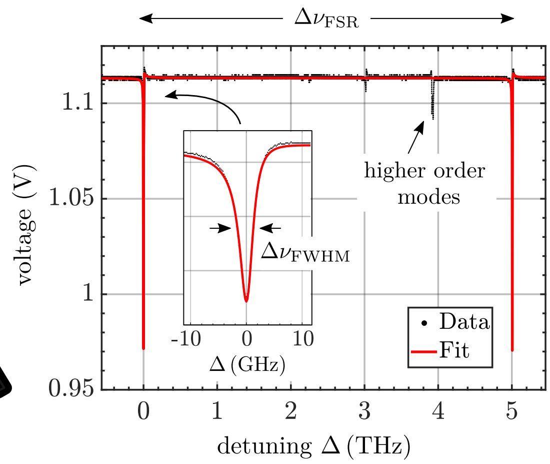

Figure 2.7: **(a)** Reflection-measurement scheme. The optical path features a $\lambda = 780\,\mathrm{nm}$ laser beam passing through a Polarizing-Beam-Splitter (PBS) into the hybrid fiber mirror cavity. The fiber mirror is stationed on a Piezo-Translation-Stage (PTS) that is driven by a triangular voltage signal produced by a function generator (WGEN). The reflection signal of the cavity is recorded with a photodiode ($\mathrm{PD}_{\mathrm{refl}}$) that is connected to an oscilloscope. **(b)** Exemplary measurement of two consecutive resonances of the fundamental mode separated by the FSR ($\Delta\nu_{\mathrm{FSR}}$) with higher-order transversal modes in-between. The two mirrors are separated by $L_{\mathrm{cav}} = (30 \pm 3)\,\mathrm{\mu m}$. For illustrative purposes, this specific cavity scan is taken with a polymer structure inside the cavity.

length to such a precise degree, a constant scan of the cavity length is needed to continuously "hit" the resonance condition. For the hybrid cavity, this is achieved by stationing the fiber mirror onto a Piezo-Translation-Stage (PTS) that is driven by an external (triangular) voltage signal to scan the z-position of the fiber mirror and therefore the overall cavity length L_{cav}. The corresponding reflection signal on the photodiode is then given by the familiar asymmetric lineshape introduced in section 2.2.2 in units of voltage vs. time. To convert the time-axis into frequency, the resonator-intrinsic frequency reference given by the FSR ($\Delta\nu_{\mathrm{FSR}} = c/2L_{\mathrm{cav}}$) can be used for calibration. The corresponding cavity length can be approximated with the help of a digital-microscope [13]. As the cavity used here is a mix of fiber-mirror and macroscopic mirror, the corresponding coupling depth of the reflection signal can be improved by ordinary mode-matching techniques to counteract misalignments of the types discussed in section 2.1.2. To that end, the flat mirror ($T_2 = 10\,\mathrm{ppm}$) is attached to a kinetic optical mount that allows to adjust the relative angles θ_x and θ_y between fiber and flat mirror. An exemplary reflection signal of a full FSR scan of the cavity is shown in Fig. 2.7 (b). It features a Finesse of $\mathcal{F} = \Delta\nu_{\mathrm{FSR}}/\Delta\nu_{\mathrm{FWHM}} = 1640 \pm 60$ with a coupling depth of $12.8\% \pm 0.3\%$.
For a well-fabricated fiber mirror with proper cavity mode-matching, Finesse-values of up to 3000 with coupling depths of up to 95% can be reached [14]. Fiber mirrors that meet these standards are then used for the later experiments.

[13] Dino-Lite Digital-Microscope (220x) mag.

[14] For these purposes, such a highly-overcoupled cavity is actually preferable, as any (minor) misalignment of the two mirrors just leads to higher coupling depths [25].

Chapter 3

Mechanics: Polymer membranes for membrane-in-the-middle resonators

In this chapter, the polymer membranes used inside the membrane-in-the-middle resonators as the mechanical constituent are established. A brief introduction to the general fabrication procedure is given, followed by an estimation of the physical properties of the membrane with finite element simulations. Finally, the optical quality of the polymer membranes is discussed.

3.1 Polymer membrane fabrication with direct laser writing

Direct laser writing Direct laser writing (DLW) is a lithography technique used to print complex three-dimensional structures. The technique utilizes photoresists that form long polymer chains due to the induced chemical photo-polymerization by exciting the molecules with a tightly focused laser beam. This allows for a very localized polymerization process, printing structures with minimal feature sizes of up to 100 nm [30]. To this end, the commercial *NanoScribe* [1] system is used to print the dielectric membranes that will be inserted into fiber-cavities to form Membrane-in-the-Middle resonators. Since the printing of these structures has mainly been outsourced to the Linden Group, a very brief overview of the printing process sufficient for the context of this thesis will follow. For further details, consider [31].

The IP-S photoresist The commercial IP-S photoresist features the highest surface quality [2] out of all the commercially available *NanoScribe* photoresists and is also utilized to print the dielectric membranes for this thesis. It mainly consists of monomers and photoinitiators, which create radicals when excited with ultraviolet light ($\lambda \approx 390\,\mathrm{nm}$). These radicals then further react with the monomer molecules to perform polymerization, forming long polymer chains which constitute the wanted geometry.
Concerning its optical properties, the IP-S resist features a refractive index n at $\lambda_0 = 780\,\mathrm{nm}$ of roughly $n(\lambda_0 = 780\,\mathrm{nm}) \approx 1.5$ (compare Fig. 3.1 (a)) after UV-curing. The corresponding absorption coefficient of the cured photoresists at 780 nm is roughly $3 \cdot 10^{-2}\,\mathrm{mm}^{-1}$ (see Fig.

[1] *NanoScribe* GmbH: https://www.nanoscribe.com/

[2] Information acquired from an E-mail exchange with a *NanoScribe* GmbH employee.

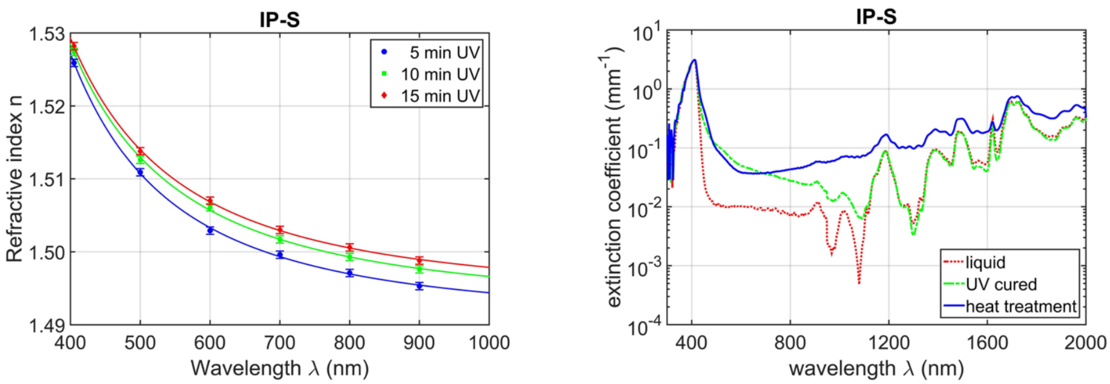

(a) (b)

Figure 3.1: **(a)** Refractive index n against wavelength λ for the IP-S photoresist. As the exposure time to UV-light increases, the refractive index increases accordingly. Here the value for n after 10 minutes of exposure time is used. **(b)** Extinction coefficient against wavelength λ for the IP-S photoresist. The green curve corresponds to the relevant data for UV-cured photoresists. Images taken from [32].

3.1 (b)). With this, absorption losses for structure thicknesses of a few microns are below 50 ppm and completely negligible compared to the transmission losses of the mirrors.

The *NanoScribe* system The DLW is performed by the commercial *NanoScribe* Professional GT (see Fig. 3.2 (a)) which utilizes a 780 nm pulsed femtosecond laser to induce polymerization via two-photon absorption at double the excitation wavelength of the photoresist [33]. The major benefit compared to the standard single-photon absorption at the excitation wavelength is due to the suppression of higher-order lobes of the (Airy) intensity pattern of the laser beam. This increases the achievable spatial resolution of the DLW technique [31].

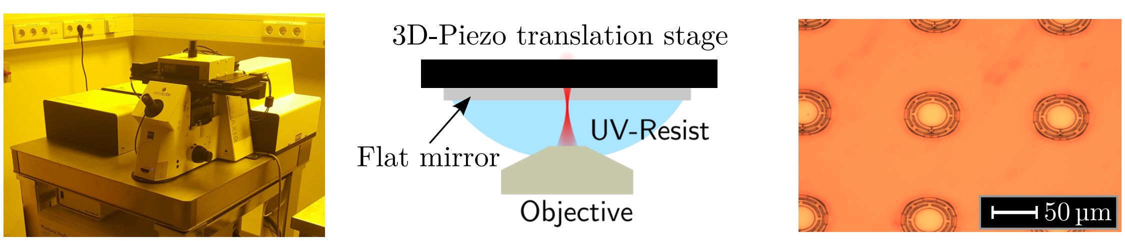

(a) (b) (c)

Figure 3.2: **(a)** *NanoScribe* system used for the DLW (taken from [31]) **(b)** Schematic of the Dip-in writing configuration (taken and edited from [31]) **(c)** Top-down view of a microscope image of a polymer drum array printed onto a substrate. Image courtesy of Alexander Faßbender.

The so-called "Dip-in" configuration is used to print the desired geometry out of the photoresist: A droplet of the liquid photoresist is placed onto a substrate (or in this case a flat mirror) which is connected to a 3D-piezo-translation stage that allows for very precise shifts of the substrate position of up to 10 nm [3] (see Fig. 3.2 (b)). The laser objective is then "dipped"

[3] The writing resolution is not limited by the precision of the piezo element but rather the confinement of the laser beam.

inside the photoresist and the laser power is increased above the polymerization threshold of the resist. This allows to locally polymerize the photoresist at the beam focus. By shifting the position of the photoresist with respect to the beam focus, the desired geometry can be printed out. After the DLW process, any unpolymerized resist is washed off, followed by an additional external UV-cure to polymerize any remaining small portions of photoresist trapped inside the already cured polymer structure. For this work, small drum or table-like structures of a few tens of microns in size are of interest for the optomechanical experiments. Fig. 3.2 (c) shows a top-down view of an exemplary print of such drum-like structures onto a substrate.

3.2 Polymer membrane geometry and *COMSOL* simulations

In this work, the optomechanical system will consist of a (fiber) Fabry-Perot cavity with integrated polymer membranes. As section 3.1 already gave a brief overview on how these polymer structures are fabricated, the focus will now be on the physical properties of the polymer (drum) membrane, especially on their eigenmodes of vibration as they form the basis for the optomechanical interaction in the later experiment. To now estimate the expected real physical parameters, finite element simulation with the multiphysics simulation software *COMSOL* [4] are performed. These then lead to the wanted eigenfrequencies Ω_m of the mechanical motion of the drum and its corresponding displacement fields $\boldsymbol{u}(x, y, z)$ (quantifying the deformation of the membrane).

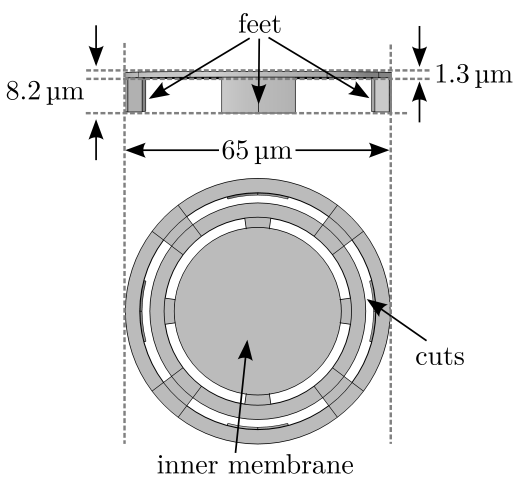

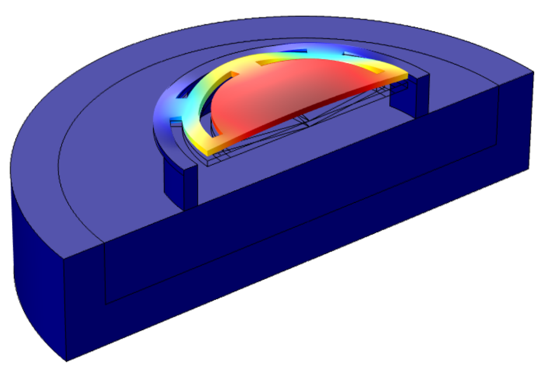

Figure 3.3: **(a)** Side and top-down view of the drum geometry **(b)** Cross-section of the drum geometry and its displacement field for the lowest order vibrational eigenmode on top of a cutout of a flat mirror. The red colored area corresponds to the maximum displacement.

For this purpose, the drum geometry (displayed in Fig. 3.3 (a)) is chosen in a way that strikes a balance between sturdiness and low effective mass (meaning higher optomechanical coupling) while also being well compatible with the optical mode of the cavity. It features a $D_{\text{out}} = 65\,\mu\text{m}$ wide and $d = 1.3\,\mu\text{m}$ thick circular membrane top with a circular-cut pattern

[4] *COMSOL* Multiphysics: https://www.comsol.com/

Q_m	Ω_m	$\Gamma_m/2\pi$	m_{eff}	E_Y	ν_P	D_{out}	D_{in}	d	L_2
$2.6 \cdot 10^6$	357 kHz	0.14 Hz	1.9 ng	2.9 GPa	0.4	65 µm	35 µm	1.3 µm	8.2 µm

Table 3.1: Results of the finite element simulation of the lowest order vibrational eigenmode of the drum. The used mechanical properties and the corresponding drum geometry are also displayed.

around the edge of the membrane, which allows for less restricted motion of the inner drum plate (roughly $D_{\text{in}} = 35\,\mu\text{m}$ in diameter). The membrane is supported by four curved feet around the membrane edge, each with a total height of about $L_2 = 8.2\,\mu\text{m}$. The whole structure sits on top of a flat mirror to form one side of the Fabry-Perot cavity. Due to the different speeds of sound in the polymer drum and flat mirror, the transfer of energy between the two is "impedance mismatched", meaning that any leakage of the vibrational energy into the flat mirror is strongly suppressed. The Young's modulus E_Y (essentially an extension of the spring stiffness of the 1D harmonic oscillator to continuous bodies) and Poisson's ratio ν_P (quantifying the deformation of the body due to axial- and transversal strain) that describe the mechanical properties of the drum are taken from [34], and collected in Tab. 3.1. It is important to note here that the mechanical properties of the photoresist are strongly dependent on the DLW fabrication process, as demonstrated in [35]. Since it is difficult to adjust these parameters to the specific writing settings to get a more accurate prediction, the simulations (as of right now) only serve as a rough guideline of what to expect in the experiment. In the future, the experimental results will then be used to draw conclusions about the actual mechanical properties of the polymer drum.
As a first step, only the fundamental eigenmode corresponding to the alternating up-and-down motion of the drum membrane is considered. The resulting displacement field describing its motion is represented in Fig. 3.3 (b). With this, the expected eigenfrequency Ω_m can be approximated. The effective mass of the mechanical mode of the drum is calculated by considering the displacements fields $\boldsymbol{u}(x, y, z)$ of the motion [36]:

$$m_{\text{eff}} = \frac{\int_V \, \mathrm{d}V \rho(x,y,z) \cdot |\mathbf{u}(x,y,z)|^2}{\max_V \left(|\mathbf{u}(x,y,z)|^2\right)}$$

with V as the full simulation volume and $\rho(x, y, z)$ as the local density. It is used to determine the zero-point-fluctuation amplitude x_{zpf} and plays an important role in approximating the optomechanical coupling later on. Since the simulations are performed in vacuum, the primary loss channel of the drum motion is just given by the internal dampening from the deformation process itself. To quantity this, the so-called mechanical quality factor $Q_m = \frac{\Omega_m}{\Gamma_m}$ is introduced, with the mechanical linewidth $\Gamma_m/2\pi$. The design of the drum membrane is chosen in a way to achieve high mechanical quality factors, but a rigorous process to find the best possible design with the highest Q_m possible has not been performed yet. Tab. 3.1 displays the relevant simulated physical parameters for the drum geometry.

3.3 Optical quality of laser written polymer structures

As a consequence of introducing dielectric objects (polymer drums) into a Fabry-Perot cavity, the optical quality of the cavity will suffer due to scattering and absorption at the dielectric. High optical quality is generally desired for optical resonators, but also especially relevant for optomechanical experiments since reaching interesting regimes such as the resolved-sideband regime [13] or the strong-coupling regime [37] is only possible with low optical losses inside the resonator. To quantify the optical quality of the resonator, the already introduced Finesse $\mathcal{F}$ (refer to section 2.1.1) is utilized. In the case of a Fabry-Perot resonator with a dielectric element placed in-between the two mirrors, the Finesse reads:

$$\mathcal{F} = \frac{2\pi}{T_1 + T_2 + L_1 + L_2 + L_{\text{clip}} + L_{\text{poly, abs}} + L_{\text{poly, scat}}} \tag{3.1}$$

with transmission losses $T_1 = 2000\,\text{ppm}$ ($T_2 = 10\,\text{ppm}$) and intrinsic coating losses $L_1 = 15\,\text{ppm}$ ($L_2 = 15\,\text{ppm}$) of mirror 1 (2) [5]. The clipping losses L_{clip} have already been introduced in Eq. (2.19). The term $L_{\text{poly, abs}} + L_{\text{poly, scat}}$ takes care of the absorption and scattering losses at the dielectric for a full cavity round-trip. As mentioned in section 3.1, the commercial *NanoScribe* photoresists feature miniscule absorption losses that can be safely neglected for feature sizes of up to a few micrometers. The main contribution to the losses from the polymer comes from light scattering at the surface of the dielectric. To quantify these losses, a test cavity system is build consisting of a fiber-mirror for in-coupling light and a flat mirror that hosts a staircase-like *NanoScribe*-printed polymer structure. It makes use of the reflection-based measurement scheme introduced in section 2.4. A schematic of the test cavity is depicted in Fig. 3.4. The staircase features 9 distinct steps, each with a $25\,\mu\text{m} \times 25\,\mu\text{m}$ surface area and step height of 50 nm (with a total height of roughly $\lambda/2$).

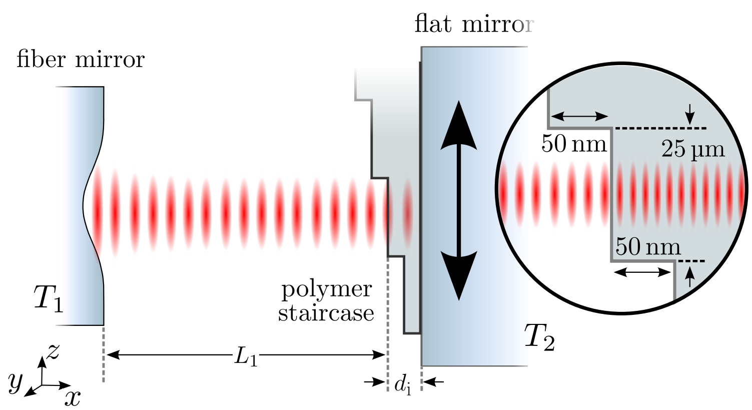

Figure 3.4: Test cavity consisting of an in-coupling fiber mirror and a flat mirror that hosts a polymer staircase. The inset depicts the geometry of the staircase. The flat mirror is attached to a motorized stage (Standa: 8MT167-25) that allows for y-z-translations of submicron precision. The cavity length $L_1 + d_i$ is kept constant at roughly 30 µm.

The idea now is to place the fiber at a specific position over the staircase, measure a cavity resonance and its corresponding Finesse and then repeat the same measurement at a different

[5] These specific transmission losses of the mirrors are selected to improve the overall impedance-matching after the polymer structures are introduced inside the cavity.

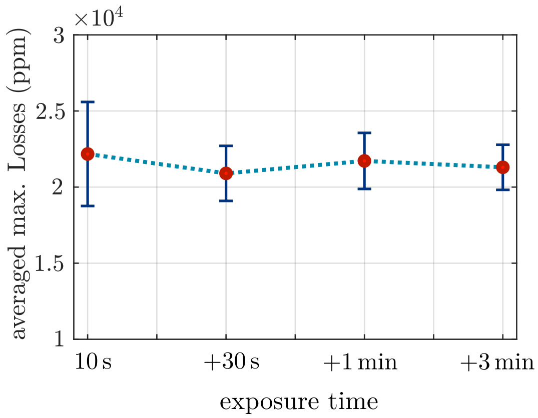

(a)

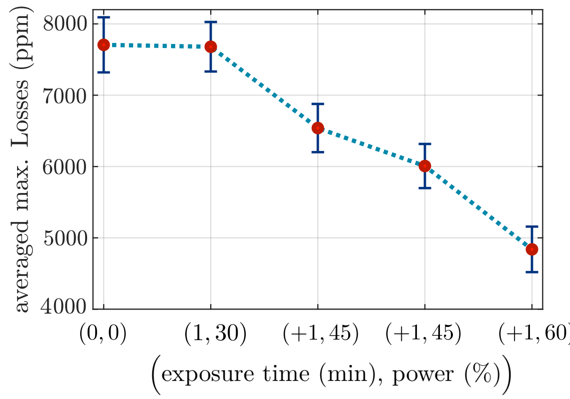

(b)

Figure 3.5: **(a)** Maximum losses of the averaged Finesse map scans for different exposure times to NMP. The x-axis is not properly scaled and represents the additional exposure time (denoted by a "+") experienced by the staircase sample. **(b)** Maximum losses of the averaged Finesse map scans for different exposure times and plasma powers with the plasma cleaner.

position on the staircase. With this, the complete surface of the staircase can be mapped to a corresponding Finesse value, effectively creating a "Finesse map" for the staircase. Since the cavity mode width ($\omega_0 \approx 3 - 4\,\mu\text{m}$) is rather large compared to the staircase dimensions, the resulting Finesse distribution will already be subject to some spatial averaging from the get-go, nevertheless the resolution obtained here is sufficient to make statements about the optical quality of the polymer structure.
Due to the $\lambda/2$-periodic intensity distribution of the cavity field, measuring the Finesse at the different steps corresponds to a different intensity of the cavity field at the dielectric surface. Since the scattering losses depend on the intensity at the scattering surface (i.e the staircase surface), the Finesse also experiences such a periodic modulation across the staircase height. The amplitude of this modulation is then directly proportional to the expected scattering losses. A Finesse map scan of a polymer staircase and the corresponding induced losses are shown in Fig. 3.6 (a). The upper part of the image depicts the spatial Finesse distribution of the staircase on the flat mirror. Each pixel stands for a measurement and every $2\,\mu\text{m}$ such a measurement is taken. It shows the expected periodic modulation of the Finesse across the length of the staircase. The expected geometry of the staircase is well reproduced, but the dimensions of the staircase in the Finesse map are generally smaller than the real-life geometry. This is mostly due to increased losses at the edge of the structure combined with the rather large cavity mode width. The latter is also most likely the reason why the individual staircase steps are not resolved in the map itself. In the lower graph, the corresponding losses (in ppm) induced by the polymer L_{poly} (here mainly scattering losses) across the length of the staircase are depicted.

The losses are averaged over the width of the staircase and any data points that clearly correspond to damage (or persistent dust and dirt accumulation) of the polymer are excluded. The situation at which the intensity is maximized at the polymer surface is most relevant for the later experiments since the coupling between optical and mechanical mode is maximized if the field is maximized at one side of the drum membrane surface (see section 4.1.4). It is therefore interesting to reduce the polymer induced losses L_{poly} at the dielectric surface for an anti-node in the cavity field (i.e maximal losses). From Fig. 3.6 (a) it is clear that the losses induced by the polymer greatly exceed any other losses of the cavity and are therefore the limiting factor on the overall Finesse. The goal now is to find ways to reduce these losses while keeping the overall geometry of the polymer structure in tact.

3.3.1 Improving the optical quality of polymer structures

To improve the optical quality of the polymer structure, two common methods for surface polishing polymer materials are employed. As a first step, the organic solvent N-Methyl-2-pyrrolidone (NMP) is used to attempt to chemically polish the polymer surface.

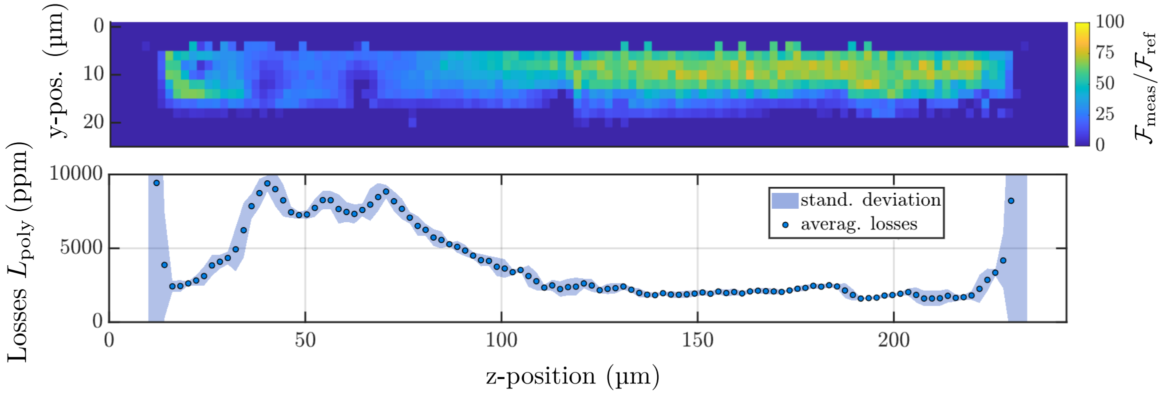

(a)

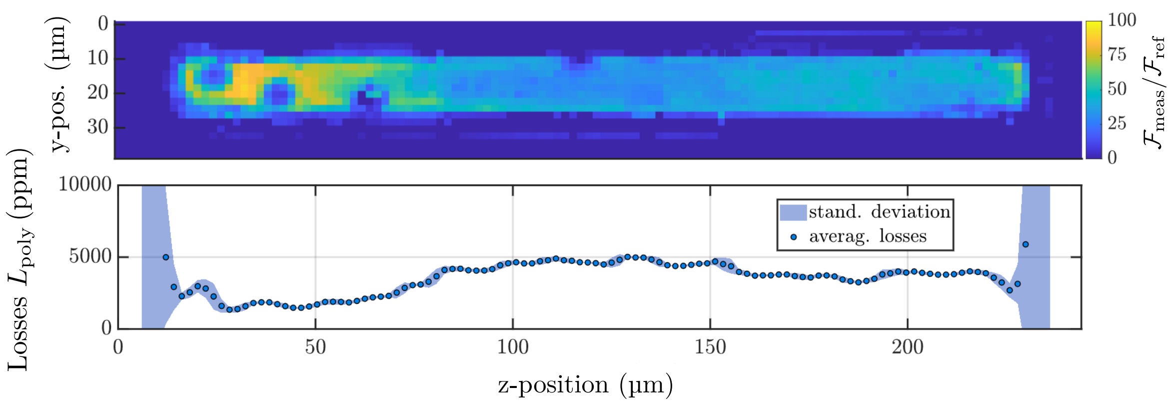

(b)

Figure 3.6: **(a)** (top) Measured Finesse $\mathcal{F}_{\text{meas}}$ on the unpolished staircase normalized by the reference Finesse $\mathcal{F}_{\text{ref}}$ without the staircase against the y-z-position on the flat mirror. Zero Finesse corresponds to a measurement of a cavity reflection resonance with coupling depth below 3% where fitting the resonance becomes unsuccessful. **(a)** (bottom) Corresponding losses induced by the polymer averaged over the width of the staircase against the z-position. The losses are calculated by measuring the Finesse and solving for the polymer losses L_{poly} in Eq. (3.1). **(b)** Same staircase sample as in (a) but polished using the plasma cleaner. The periodicity of the Finesse across the z-position is somewhat lost at the end of the staircase sample hinting at a non-linear polymer removal of the staircase due to e.g unwanted charge accumulation.

A staircase sample is progressively exposed to NMP for certain exposure times. After each exposure, a Finesse map is taken to quantify the effects of the chemical on the staircase.

The resulting maximum losses of the averaged Finesse against the exposure time to NMP are displayed in Fig. 3.5 (a). From this, it is clear that the NMP did not have the desired effect [6] and the Finesse maps after each consecutive NMP exposure barely showed any change. Increasing the exposure times even further only leads to the staircase detaching from the flat mirror.
As a second step, a low-pressure plasma cleaner device [7] is utilized. A plasma source generates highly reactive chemicals from O_2. The resulting chemicals (dubbed reactive oxygen species) occupy free chain ends of the polymer to create degradation products such as CO_2 that can be easily removed afterwards. This improves the surface roughness of the staircase samples and therefore reduces the losses due to light scattering. The same sample already introduced in Fig. 3.6 (a) is then progressively exposed to the plasma cleaner for certain exposure times and plasma powers. A Finesse map of the sample after the final treatment step is displayed in Fig. 3.6 (b). Compared to the untreated sample, it features a more homogeneous Finesse distribution and also a shift of the position of maximum Finesse. This is due to the removal of the first few surface layers of the staircase by the plasma cleaner, as it is reducing the overall staircase height by a few nanometers. The resulting maximal losses for all of the treatment steps are depicted in Fig. 3.5 (b). Due to time constraints, the surface polishing could not be further continued beyond this first testing and the full potential of this technique for surface polishing the polymer structures is not yet fully known. Nevertheless, the maximum losses are reduced by more than 30% by the plasma cleaning procedure, which already shows promise in improving the optical quality of the polymer structures.

[6] The NMP might polish the surface at too small of a scale to affect the optical quality of the polymer and is thus not measurable here.

[7] diener electronic: Zepto 119167

Chapter 4

Optomechanics: Cavity optomechanics with polymer membranes

The field of cavity optomechanics explores the interaction between electromagnetic radiation and mechanical motion in optical resonators. Here, a novel platform that uses a "Membrane-in-the-Middle" (MIM) configuration is studied. It consists of a dielectric membrane (the mechanical resonator) inserted between the two mirrors of a Fabry-Perot cavity (hosting optical resonator modes). While some MIM experiments also make use of fiber mirrors to build MIM cavities ([38], [39]), most experiments utilize (commercial) silicon nitride membranes as the mechanical constituent that is integrated into the optical cavity system. These membranes offer favorable mechanical and optical properties as required for optomechanical experiments. Here, a different approach is pursued: laser written polymer membranes (drums) are utilized as the mechanical resonator element. The extreme flexibility of the laser writing process allows for direct integration of the mechanical resonator into the microscopic cavity and the direct fiber coupling offers great interfacing capabilities.
The goal of this thesis is to show a proof of principle operation of this novel MIM system and also determining its optomechanical coupling strength. The following sections give an overview of the novel optomechanical system, the expected coupling, the measurement setup and the experimental characterization of the system.

4.1 The optomechanical interaction

First, this section presents the MIM optomechanical system that was developed during this thesis and introduces the basics of the optomechanical interaction. Next, the coupling mechanism responsible for the interaction in this system is explained and the corresponding calculations to approximate the coupling strength are detailed.

4.1.1 A membrane-in-the-middle resonator

The MIM system consists of a cavity that is confined by two mirrors with a dielectric membrane in-between. For a graphical representation of the cavity geometry, see Fig. 4.1 (a). Here, the in-coupling mirror consists of an end facet of a single-mode fiber with a concave center area created via laser ablation (see Fig. 4.1 (c)). The fiber end facet is covered with a reflective coating to form a Bragg-mirror (for details, refer to section 2.3) with transmission losses of $T_1 \approx 2000$ ppm. Typical single-mode fiber diameters are in the range of 125 µm, with fiber-core diameters of a few microns. Opposing the fiber mirror is a 0.5 inch flat mirror with $T_2 \approx 10$ ppm transmission. These parameters have been chosen to improve the impedance-matching of the resulting MIM cavity since the polymer membrane will inevitably introduce further losses into the resonator on the order of some 100 to 1000 ppm (refer back to section 3.3).

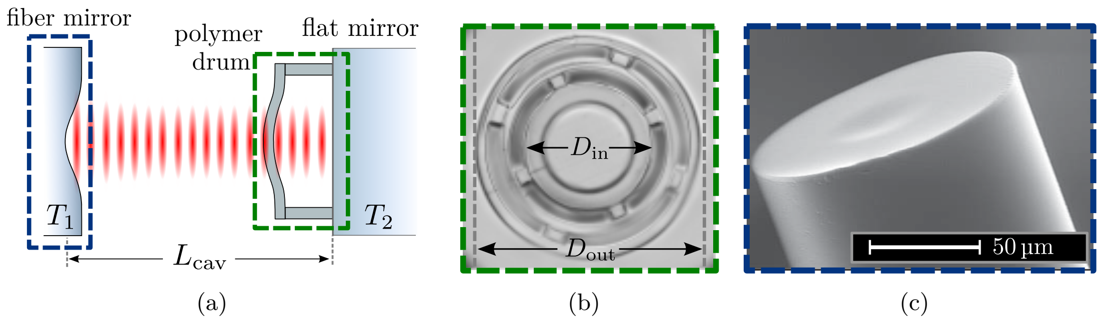

Figure 4.1: **(a)** Schematic diagram of the geometry of the MIM-resonator. It features two opposing mirrors: a fiber mirror (with transmission T_1) used for in-coupling light into the resonator (blue dashed border) and a flat mirror (with transmission T_2), hosting the polymer drum structure (green dashed border) at a spatial separation of L_{cav}. **(b)** Top-down view of a printed polymer drum structure corresponding to the green dashed border in (a). Two main lengths define the overall geometry of the drum structure: the inner drum membrane diameter $D_{\text{in}} \approx 35$ µm and the total drum diameter $D_{\text{out}} \approx 65$ µm. Image courtesy of Alexander Faßbender. **(c)** SEM image of a typical fiber mirror corresponding to the blue dashed border in image (a). It features a small spherical depression shot onto the fiber-end facet that acts as a spherical mirror when covered with reflective coating. Image taken from [16].

The hybrid cavity (fiber mirror plus flat macroscopic mirror) is chosen since the flat mirror offers more flexibility to print multiple different *NanoScribe* polymer structures on just one single optical element for first characterization purposes. Later on a complete FFPC based realization is planned. The membrane used in the MIM setup is a *NanoScribe*-written dielectric polymer drum, described in detail in section 3.2. An image of the drum geometry is shown in Fig. 4.1 (b). It features cuts on the membrane, such that the inner drum part is only connected to the supporting frame by small tethers. These are introduced to increase the expected mechanical quality factor Q_{mech}. Supporting feet (roughly 8 µm tall) hold up the membrane and rest on the flat mirror. The coupling of the suspended membrane to the optical cavity field is discussed in the following sections.

4.1.2 Hamiltonian formulation

To describe the coupled system of electromagnetic radiation and mechanical motion, a Hamiltonian formulation is applied [13]. În our case, the radiation mode is given by an optical eigenmode of the FFPC [1]. The mechanical motion that interacts with the optical field is provided by the vibration of a semi-transparent dielectric membrane. However, in a first step, a generic "mirror-on-a-spring" system is discussed, as this simple system sufficiently describes

[1]Microwave modes (eg. in an LC circuit) are also very commonly used to couple to mechanical motion and constitute the branch of Microwave-Optomechanics.

the optomechanical interaction and most optomechanical systems can be mapped to the same Hamiltonian. A pictorial representation of this system is depicted in Fig. 4.2. The uncoupled optical (ω_{cav}) and mechanical (Ω_m) modes [2] within this model are represented by two harmonic oscillators (ignoring their zero-point energy contributions) in the bare Hamiltonian:

$$\hat{H}_0 = \hbar\omega_{\text{cav}}\hat{a}^\dagger\hat{a} + \hbar\Omega_m\hat{b}^\dagger\hat{b} \tag{4.1}$$

with photonic (phononic) annihilation and creation operators $\hat{a}$ ($\hat{b}$) and $\hat{a}^\dagger$ ($\hat{b}^\dagger$) obeying the standard commutation relation $\left[\hat{a}, \hat{a}^\dagger\right] = 1$ $\left(\left[\hat{b}, \hat{b}^\dagger\right] = 1\right)$. The mechanical resonance frequency is fixed at Ω_m, but the optical frequency ω_{cav} in this picture is a function of the position x of the mechanical resonator.

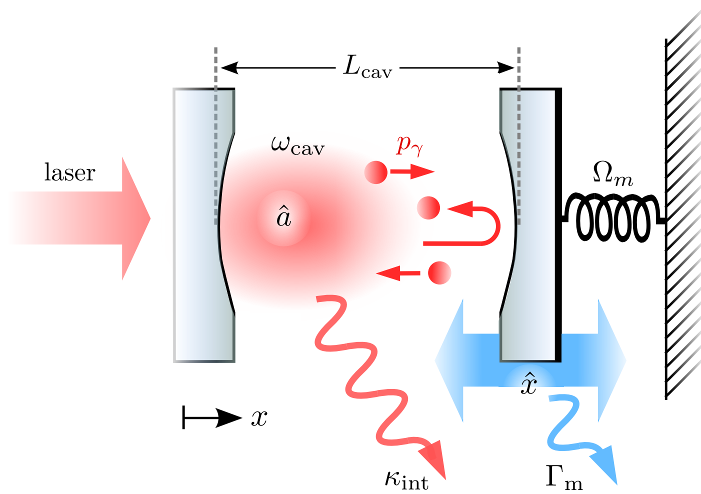

Figure 4.2: Schematic representation of a generic "mirror-on-a-spring" optomechanical system. It features the optical mode $\hat{a}$ with resonance frequency ω_{cav} confined in a Fabry-Perot resonator consisting of two opposing highly reflective mirrors separated by L_{cav}. One of the mirrors is anchored to the wall via a spring. The mechanical oscillator displacement is given by $\hat{x}$ with its mechanical frequency Ω_m. Both the optical and mechanical modes are coupled to external loss channels. Here the optical loss channel is indicated by the cavity photon decay rate κ_{int} while the mechanical loss channel is indicated by the dampening rate Γ_m. Radiation pressure given by the photon momentum p_γ acts on the movable end-mirror. On the other hand, the displacement of the mirror acts back on the optical resonance frequency giving rise to the optomechanical coupling.

Expanding the optical frequency $\omega_{\text{cav}}(x)$ to first order, as is sufficient for most experimental realizations of optomechanical cavities [3], one finds:

$$\omega_{\text{cav}}\,(x) \approx \omega_{\text{cav}}\, + x\partial\omega_{\text{cav}}\,/\partial x + \cdots \tag{4.2}$$

where $G^{(1)} = -\partial\omega_{\text{cav}}/\partial x$ [4] defines the so called linear frequency-pull parameter [13], i.e. quantifying the frequency shift of the optical resonance frequency $\mathrm{d}\omega_{\text{cav}}$ induced by a given

[2] Here, one only considers one mode each for the mechanical and optical degree of freedom, extensions to higher orders are also viable but not needed for the theoretical context of this thesis.

[3] The second-order term does become interesting for MIM-experiments as quantum non-demolitions measurements of the mechanical phonon occupation have been proposed [40] in systems with negligible linear coupling.

[4] The minus sign assures that the frequency decreases when applying a positive ($x > 0$) shift of the movable mirror position

spatial shift of the mechanical oscillator dx. For a simple "mirror-on-a-spring" cavity of length L_{cav}, one finds $G^{(1)} = \omega_{\text{cav}}/L_{\text{cav}}$. Hence, miniaturized cavities with small cavity lengths L_{cav} increase the frequency shift induced on the optical mode.

In MIM systems the frequency shift of the optical mode is not caused by a moving end mirror but by the displacement of the intra-cavity membrane. This calculation of the frequency pull parameter for this case is detailed in section 4.1.4. Expanding the linear terms in the Hamiltonian (Eq. (4.1)) to first-order now leads to:

$$\hat{H} = \hbar(\omega_{\text{cav}} - G\hat{x})\hat{a}^\dagger\hat{a} + \hbar\Omega_m\hat{b}^\dagger\hat{b}.$$

Here the position operator $\hat{x}$ can be decomposed into a sum of the phononic creation and anhiliation operators $\hat{x} = x_{\text{ZPF}}\left(\hat{b} + \hat{b}^\dagger\right)$ where the zero-point-fluctuation amplitude has been introduced [22]:

$$x_{\text{ZPF}} = \sqrt{\frac{\hbar}{2m_{\text{eff}}\Omega_m}}.$$

Here, m_{eff} is the effective mass of the mechanical mode. Finite element simulations of the mechanical resonator can be used to extract the value of m_{eff} (see section 3.2). The full Hamiltonian, including the interaction term (but not including laser drive and decay terms), now reads:

$$\hat{H} = \hat{H}_0 + \hat{H}_{\text{int}} = \hbar\omega_{\text{cav}}\hat{a}^\dagger\hat{a} + \hbar\Omega_m\hat{b}^\dagger\hat{b} - \hbar g_0\hat{a}^\dagger\hat{a}\left(\hat{b} + \hat{b}^\dagger\right), \tag{4.3}$$

where

$$g_0^{(1)} = G^{(1)}x_{\text{zpf}} \tag{4.4}$$

is the linear vacuum optomechanical coupling strength (from now on the superscript (1) will be dropped, unless required for visual clarity) with units of frequency. It describes the frequency shift of the cavity per zero-point displacement of the mechanical resonator; it also quantifies the force exerted onto the end mirror per intra-cavity photon [5]. It is one of the main figures of merit for optomechanical systems and its measurement will play a major role in this thesis.

The optomechanical coupling g_0 is typically very small compared to any incoherent optical loss processes κ_{int}. To remedy this, a large number of photons n_{cav} must populate the cavity as can be realized with a bright pump field. Mathematically, this corresponds to "linearizing" the interaction term of the optomechanical Hamiltonian [41] (see Eq. (4.3)). To this end, the cavity field $\hat{a}$ is split up into a mean field amplitude $\langle\hat{a}\rangle = \bar{\alpha}$ with $|\bar{\alpha}| \gg 1$ and a small fluctuating part $\delta\hat{a}$ that describes deviations away from the mean field:

$$\hat{a} = \bar{\alpha} + \delta\hat{a} \tag{4.5}$$

With this expansion, products of fluctuation operators may be dropped as:

$$\begin{aligned}\hat{a}^\dagger\hat{a} &= \bar{\alpha}^2 + \bar{\alpha}\left(\delta\hat{a}^\dagger + \delta\hat{a}\right) + \delta\hat{a}^\dagger\delta\hat{a} \\ &\approx \bar{\alpha}^2 + \bar{\alpha}\left(\delta\hat{a}^\dagger + \delta\hat{a}\right).\end{aligned}$$

[5] More precisely, the radiation-pressure force is given by $\hat{F} = -\frac{d\hat{H}_{\text{int}}}{d\hat{x}} = \hbar G\hat{a}^\dagger\hat{a}$.

Inserting this expression into the interaction term of the full Hamiltonian Eq. (4.3) reads:

$$\hat{H}_{\text{int}}^{(\text{lin})} = -\hbar\omega_{\text{cav}}|\bar{a}|^2(\hat{b}+\hat{b}^\dagger) - \hbar g_0\sqrt{\bar{n}_{\text{cav}}}\left(\delta\hat{a}^\dagger + \delta\hat{a}\right)\left(\hat{b}+\hat{b}^\dagger\right). \tag{4.6}$$

The first term in Eq. (4.6) indicates the existence of a mean radiation pressure force $\bar{F} = -\frac{d\hat{H}_{\text{int,first}}}{d\hat{x}} = \hbar G|\bar{a}|^2$. For simplification, the origin position of the mechanical resonator is shifted by $\Delta\bar{x} = \bar{F}/m_{\text{eff}}\Omega_m^2$ to eliminate this contribution from the interaction Hamiltonian. In this form the original vacuum linear coupling strength g_0 has been boosted to $g_0 \cdot \sqrt{\bar{n}_{\text{cav}}}$ by the average photon number inside the cavity. This means that the effective optomechanical coupling can be amplified by pumping the cavity with high laser intensities. Nevertheless, g_0 remains the fundamental figure of merit quantifying the coupling strength for a single photon ($\bar{n}_{\text{cav}} = 1$).

This linearization scheme can also be applied for moderate photon numbers $\bar{n}_{\text{cav}}$ circulating inside the resonator [13]. Especially for low Finesse cavities (as is the case for this thesis) with high optical decay rates (i.e. a small average photon lifetime) [6] the mechanical resonator is not able to resolve the contributions from each individual cavity photon.

[6]In this context, the photon lifetime ($\propto \frac{1}{\kappa}$) describes how long a photon stays inside the cavity before inevitably decaying out of the cavity through loss channels (such as transmission, scattering or absorption of the photon) denoted by κ.

4.1.3 Fields inside membrane-in-the-middle cavities

To calculate the optomechanical coupling strength g_0 (from Eq. (4.4)) in a MIM-cavity, considerations about the field inside the cavity have to be made. For this purpose, a purely classical analysis of the electric and magnetic fields with the help of Maxwell's Equations [42] is sufficient.
Consider the simplified geometry of the "Air-Membrane-Air" cavity and its corresponding field distribution, illustrated in Fig. 4.3. In this simplified picture, the cavity consists of a non-dispersive and loss-less dielectric with refractive index n, which is placed between two mirrors with a perfectly conducting surface, enforcing field nodes at their positions. The geometry of the cavity and its field distribution is completely determined by the free-space cavity length L_1 defined by the left in-coupling mirror M_1 at $x = x_1$ and left membrane edge at $x = 0$, the membrane thickness d defined by the left (right) membrane edge at $x = 0$ ($x = x_0$) and leg height L_2 defined by the right membrane edge at $x = x_0$ and right mirror M_2 at $x = x_2$.

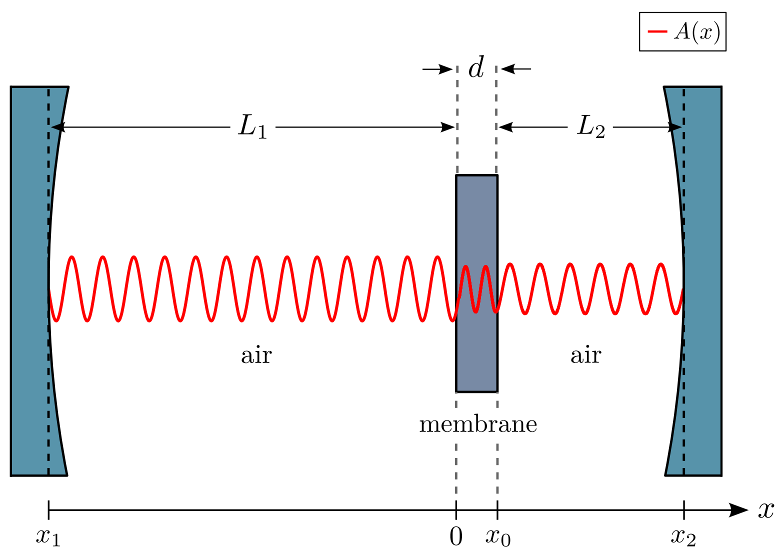

Figure 4.3: Field $A(x)$ inside "Air-Membrane-Air" cavity split into the fields $A_L(x)$ spanning across free-space length L_1, $A_M(x)$ across the membrane thickness d and $A_R(x)$ spanning across leg length L_2. The field is confined by two (assumed) perfect electrical conductors surrounded by air, mirror 1 located at $x_1 = -L_1$ and mirror 2 located at $x_2 = L_2 + d$. The dielectric membrane region is confined to $0 \leq x \leq x_0 = d$.

As a first step, the Gaussian-beam envelope is assumed to be only slowly varying across the cavity length and the standard plane-wave ansatz is made. For ease of notation, all considerations for the electric and magnetic fields are expressed in terms of the vector potential $\boldsymbol{A}(\boldsymbol{r}, \omega)$. In source-free-space, the vector potential $\boldsymbol{A}(\boldsymbol{r}, \omega)$ constitutes the fields as [42]:

$$\boldsymbol{E}(\boldsymbol{r}, \omega) = -i\omega\, \boldsymbol{A}(\boldsymbol{r}, \omega) \tag{4.7}$$

$$\boldsymbol{H}(\boldsymbol{r}, \omega) = \frac{1}{\mu} \nabla \times \boldsymbol{A}(\boldsymbol{r}, \omega) \tag{4.8}$$

with magnetic permeability μ of the membrane medium. Suppressing the explicit frequency dependence of the fields and assuming a linearly polarized field in the z-direction and propagating along the x-direction (see Fig. 4.3), a standing-wave ansatz can be made by splitting up the total field $A(x)$ across three respective regions according to:

$$A(x) = \begin{cases} a_L \cdot e^{ik_0 \cdot x} + b_L \cdot e^{-ik_0 \cdot x}, & -L_1 \leq x < 0 \\ a_M \cdot e^{ik \cdot x} + b_M \cdot e^{-ik \cdot x}, & 0 \leq x \leq d \\ a_R \cdot e^{ik_0 \cdot x} + b_R \cdot e^{-ik_0 \cdot x}, & d < x \leq L_2 + d \end{cases}$$

with bare angular wave number $k_0 = \frac{\omega}{c}$, dielectric angular wave number $k = n \cdot k_0$ and corresponding field amplitudes a_x and b_x. Since the tangential component of the electric field $\boldsymbol{E}(\boldsymbol{r}, \omega)$ at both surfaces of mirror 1 and 2 modeled by a perfect conductor vanishes and the tangential components of both the electric and magnetic fields ($\boldsymbol{E}(\boldsymbol{r}, \omega)$ & $\boldsymbol{H}(\boldsymbol{r}, \omega)$) need to be continuous at the interface between two dielectric media [43], boundary (and continuity) conditions can be imposed onto the field $A(x, t)$:

(I) $\frac{\partial}{\partial t} A_L(x_1, t) = 0$

(II) $\frac{\partial}{\partial t} A_R(x_2, t) = 0$

(III) $\frac{\partial}{\partial t} A_L(0, t) = \frac{\partial}{\partial t} A_M(0, t)$

(IV) $\frac{\partial}{\partial t} A_M(x_0, t) = \frac{\partial}{\partial t} A_R(x_0, t)$

(V) $\frac{\partial}{\partial x} A_L(x, t)\Big|_{x=0} = \frac{\partial}{\partial x} A_M(x, t)\Big|_{x=0}$

(VI) $\frac{\partial}{\partial x} A_M(x, t)\Big|_{x=x_0} = \frac{\partial}{\partial z} A_R(x, t)\Big|_{x=x_0}$

Applying these conditions to the standing wave ansatz for $A(x)$, a resonance condition can be formulated, relating the length parameters L_1, L_2 and d that permit a resonant cavity mode. One finds that the condition that fixes the $(L1, L2, d)$-triplet for a cavity resonant with probe light $\lambda = \frac{2\pi}{k_0}$ is given by $R_{\text{mim}}(L1, L2, d) = 0$ where:

$$R_{\text{mim}}(L_1, L_2, d) = A_+(L_1) \cdot e^{-ink_0 d} - A_-(L_2) \cdot e^{ink_0 d} \tag{4.9}$$

with coefficients $A_\pm(L)$:

$$A_\pm(L) = \frac{1 \mp in \cdot \tan(k_0 L)}{1 \pm in \cdot \tan(k_0 L)}.$$

One of the triplet parameters fixes the resonance condition, whereas the other two can be numerically extracted. An example is shown in Fig. 4.4 for $(L2, L1)$-pairs with fixed membrane thickness $d = 1\,\mu\text{m}$.

Finally, the vector potential $A(x)$ and equivalently the electric (Eq. (4.7)) and magnetic field (Eq. (4.8)) can be calculated. The vector potential $A(x)$ reads:

$$A(x) = A_0 \times \begin{cases} \frac{\sin\left(k_0(x+L_1)\right)}{i\sin(k_0 L_1) + 1/n \cdot \cos(k_0 L_1)}, & -L_1 \leq x < 0 \\ \frac{\sin(kx) + n \cdot \tan(k_0 L_1)\cos(kx)}{1 + in \cdot \tan(k_0 L_1)}, & 0 \leq x \leq d \\ \frac{e^{ikd}\,\sin\left(k_0(x-(L_2+d))\right)}{-i\sin(k_0 L_2) + 1/n \cdot \cos(k_0 L_2)}, & d < x \leq L_2 + d \end{cases} \tag{4.10}$$

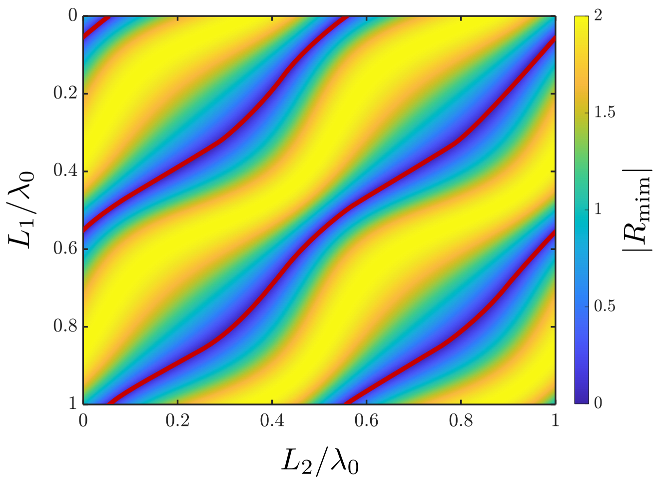

Figure 4.4: Resonant cavity condition (absolute value of Eq. (4.9)) plotted against free-space length L_1 and leg length L_2 normalized by $\lambda_0 = 780\,\mu\mathrm{m}$, with fixed drum thickness $d = 1\,\mu\mathrm{m}$. The red resonance lines show all points that are zero, i.e fulfill the condition and are periodic in L_2 and L_1 with $\lambda_0/2$.

4.1.4 Calculating the optomechanical coupling strength

In this section, the results from section 4.1.3 are used to determine the (vacuum) linear optomechanical coupling strength for the MIM system presented in this thesis. To recapitulate, the cavity resonance frequency ω_{cav} given by Eq. (4.2) and, including terms of order $\mathcal{O}(x^2)$, reads:

$$\omega_{\mathrm{cav}}\,(x) \approx \omega_{\mathrm{cav}}\; + x\frac{\partial \omega_{\mathrm{cav}}}{\partial x} + \frac{1}{2}x^2\frac{\partial^2 \omega_{\mathrm{cav}}}{\partial x^2} + \cdots \tag{4.11}$$

Where the linear coupling strength is given by $g_0^{(1)} = G^{(1)}x_{\mathrm{zpf}}$ with the linear frequency-pull parameter $G^{(1)} = \frac{\partial \omega_{\mathrm{cav}}}{\partial x}$ and the newly introduced quadratic coupling strength $g_0^{(2)} = \frac{1}{2}G^{(2)}x_{\mathrm{zpf}}^2$ with its quadratic frequency-pull parameter $G^{(2)} = \frac{\partial^2 \omega_{\mathrm{cav}}}{\partial x^2}$. Since the expected zero-point fluctuation amplitude x_{zpf} will be extracted from finite element simulations (refer to chapter 3.2), the only quantity that remains unknown is the frequency-pull parameter $G^{(1)}$ ($G^{(2)}$) and will be calculated in the following.

In a MIM system the motion of the dielectric membrane causes a dispersive shift of the cavity frequency. In contrast to the "mirror-on-a-spring" optomechanical cavity, where the geometric length of the cavity is changed, here only the effective optical length is modified. Thermal occupation of the phononic modes of the drum induces vibrational motion of the membrane at its eigenfrequencies [7]. First, the fundamental flexural mode is considered (denoted by (2) in Fig. 4.5 (b)). For this specific mode, L_1 and L_2 are decreasing and increasing respectively, while the drum membrane thickness d stays constant (compare Fig. 4.5 (a)). The cavity field experiences an effective change of the refractive index at the boundaries of the dielectric membrane, hence inducing a dispersive shift of the resonance frequency. Two methods to calculate the frequency-pull factor $G^{(1)}$ are presented: the first, straightforward method is considering the shift of the cavity geometry due to the motion of the membrane. The

[7] Even if the mechanical membrane is cooled to its motional ground-state, the zero-point fluctuations of the harmonic oscillator would cause motion of the membrane and therefore induce frequency noise in the optical cavity

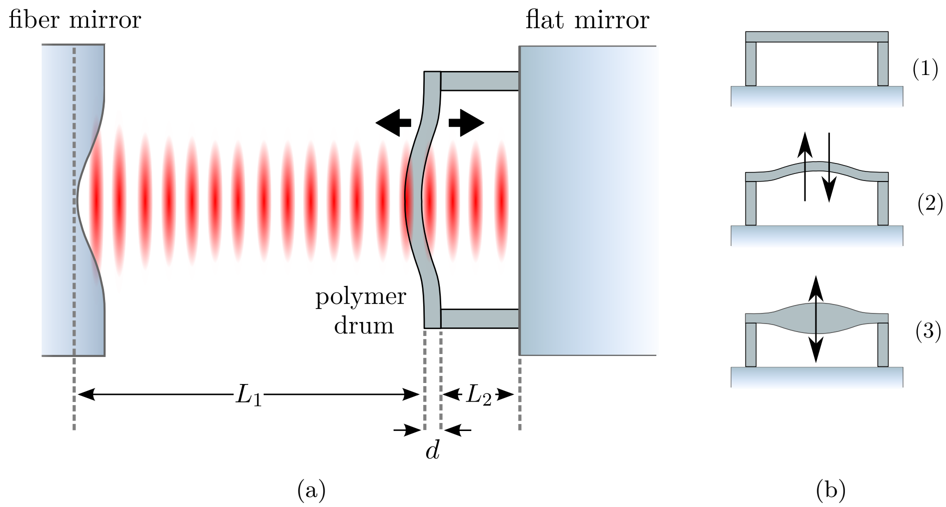

Figure 4.5: **(a)** Schematic displaying the typical geometry of the MIM-cavity. **(b)** Two of the many possible vibrational modes are displayed: (1) side view of the simplified drum geometry without vibrations. (2) the fundamental flexural mode, a periodic up-and-down motion of the drum membrane (3) a "breathing" mode, the membrane performs a periodic contraction and expansion of its thickness.

second method considers shifting material boundaries using perturbation theory for Maxwell's equations.

Method 1: The geometric approach The change of the cavity geometry induced by the vibrational motion of the membrane leads to a shift of the optical resonance frequency. To include this into the existing model that determines the allowed $(L1, L2, d)$-triplet for a given input wavelength λ_0, the following change of variables is performed:

$$\begin{cases} L_1 \to L_1 + \Delta L \\ L_2 \to L_2 - \Delta L \\ k_0 \to k_0 + \Delta k \end{cases}$$

Inserting these back into the resonance condition (Eq. 4.9) allows to numerically extract the shift Δk of the angular wavenumber and thereby the shift on the resonance frequency $\Delta\omega_{\text{cav}}$ in air. Calculating the ratio between frequency- and displacement-shift allows to determine the frequency-pull parameter $G^{(1)}$. It should be noted that these calculations consider a very simplified model to estimate frequency-pull parameter $G^{(1)}$. However, the following requirements ensure that this model determines the frequency-pull parameter $G^{(1)}$ in good approximation:

- The Rayleigh length z_R (here $z_R \approx 50\,\mu\text{m}$) has to be in the same order of magnitude as the cavity length L_{cav} (here $L_{\text{cav}} \approx 30\,\mu\text{m}$) to justify neglecting the Gaussian-beam properties of the laser light.
- The mode width ω_0 (here $\omega_0 \approx 3.5\,\mu\text{m}$) of the optical mode has to be sufficiently smaller than the effective membrane radius r_{mem} (here $r_{\text{mem}} \approx 20\,\mu\text{m}$) to ensure that the optical mode only overlaps with an almost constant displacement of the drum membrane at the center.

- The mirrors are assumed to be non-dispersive, such that the total cavity length is only given by the geometry of the cavity.

An exemplary graph displaying $G^{(1)}$ in dependence on the drum geometry normalized by the wavelength λ_0 is shown in Fig. 4.6 (a). It features a periodic pattern of well-defined minima and maxima with a periodicity of half of the material wavelength. This "coupling map" now precisely shows which (L_2, d)-pair [8] results in maximum optomechanical coupling and is used as a guideline for the drum fabrication process. The asymmetry between the minimum and maximum value arises from the fact that the cavity geometry is chosen such that the free-space cavity length L_1 is roughly double in size compared to the leg height L_2, as in the actual experiment (for more details, see Eq. (4.16) in the following paragraph).

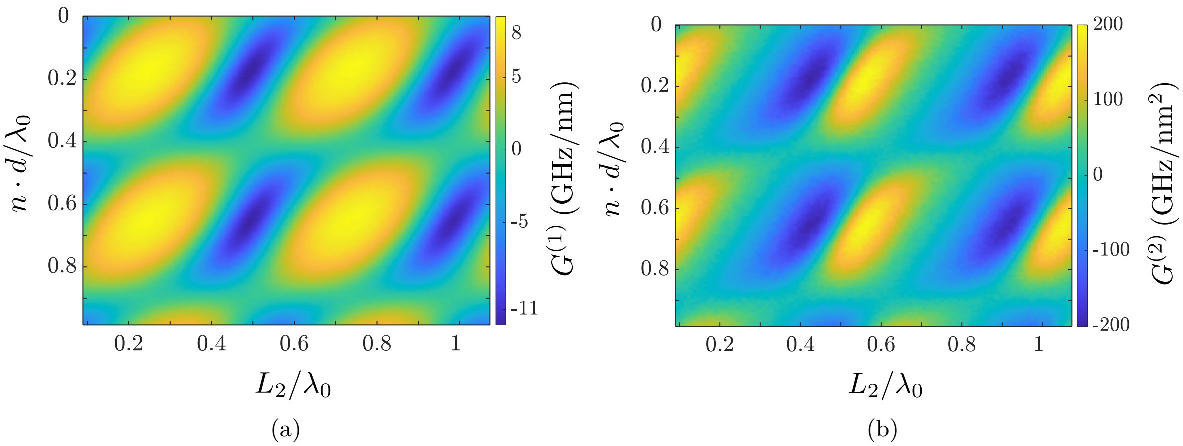

Figure 4.6: **(a)** Coupling map for $G^{(1)}$ vs. the normalized drum membrane thickness d and leg height L_2. The map features a repeating pattern with a periodicity of half of the material wavelength **(b)** coupling map for $G^{(2)}$ vs. the normalized drum membrane thickness d and leg height L_2. It is derived from (a) by a numeric derivative and also features the same periodicity as in (a).

Furthermore, the quadratic frequency-pull $G^{(2)}$ that arises as the numerical derivative of the first order frequency-pull is displayed in Fig. 4.6 (b). A unique feature that differentiates MIM systems from simple mirror-on-a-spring-like cavities is that for zero linear optomechanical coupling strength the quadratic coupling strength can be maximized (compare Fig. 4.6). With this, the effective optomechanical coupling between the optical and mechanical modes is solely given by the quadratic interaction. The interaction Hamiltonian for such a system then reads [13]:

$$\hat{H}_{\text{int}} = \hbar g_0^{(2)} \left(\hat{b} + \hat{b}^\dagger\right)^2 \hat{a}^\dagger \hat{a}$$

By invoking the Rotating-Wave-Approximation, dropping any fast oscillating terms [44], the interaction Hamiltonian $\hat{H}_{\text{int}}$ is then directly proportional to the phonon number $\hat{n}_{\text{phonon}} = \hat{b}^\dagger \hat{b}$. The quadratic optomechanical coupling could then, in principle, lead to Quantum-Non-Demolition (QND) measurements of the phonon number and generation of mechanical cat-states of the mechanical resonator [40], [13].

[8] The missing parameter of the triplet L_1 is always chosen in a way such that the overall cavity size $L_{\text{cav}} = L_1 + L_2 + d$ stays roughly constant, up to a slight deviation to always fulfill resonance.

Method 2: The pertubative approach To calculate the frequency shift per displacement $G^{(1)}$ in a perturbative context (i.e how a spatial shift of the dielectric membrane induces higher-order corrections to the resonance frequency), the framework of Maxwell's Equations written as an eigenproblem is utilized [45]. To this end, the eigenequation of the electric cavity field $\left|E^{(n)}\right\rangle$ with eigenfrequency ω_{cav} is given by the well-known wave equation in a source-free medium with dielectric permittivity $\epsilon(x)$:

$$\boldsymbol{\nabla}^2|E\rangle = \left(\frac{\omega_{\text{cav}}}{c}\right)^2 \epsilon(x)\,|E\rangle \tag{4.12}$$

For convenience, the basis-independent representation of the electric field as "Bra"- and "Ket"-vectors is utilized, with the typical inner product $\langle E \mid E'\rangle \equiv \int \mathbf{E}^* \cdot \mathbf{E}' dV$ familiar from standard quantum mechanics literature [22]. Because of the vibrational motion of the drum membrane, the effective dielectric permittivity experiences a small change $\Delta\hat{\epsilon}$ due to a perturbative shift in the position of the drum membrane Δx. With this, the new eigensolutions of the electric field and its eigenfrequencies are expanded in powers n of Δx and, to first order, lead to:

$$|E\rangle = \sum_{n=0}^{\infty} \left|E^{(n)}\right\rangle = \left|E^{(0)}\right\rangle + \left|E^{(1)}\right\rangle + \mathcal{O}(\Delta x^2) \tag{4.13}$$

$$\omega_{\text{cav}} = \sum_{n=0}^{\infty} \omega_{\text{cav}}^{(n)} = \omega_{\text{cav}}^{(0)} + \omega_{\text{cav}}^{(1)} + \mathcal{O}(\Delta x^2) \tag{4.14}$$

Inserting Eq. (4.13) and Eq. (4.14) back into Eq. (4.12) and neglecting any terms of quadratic-order leads to the first-order correction to the resonator frequency $\omega_{\text{cav}}^{(1)}$

$$\omega_{\text{cav}}^{(1)} = -\frac{\omega_{\text{cav}}^{(0)}}{2} \frac{\left\langle E^{(0)}|\Delta\epsilon|E^{(0)}\right\rangle}{\left\langle E^{(0)}|\epsilon|E^{(0)}\right\rangle}$$

or equivalently in its differential form:

$$G^{(1)} = \frac{d\omega_{\text{cav}}}{dx} = -\frac{\omega_{\text{cav}}^{(0)}}{2} \frac{\left\langle E^{(0)} \left| \frac{d\epsilon}{dx} \right| E^{(0)}\right\rangle}{\left\langle E^{(0)}|\epsilon|E^{(0)}\right\rangle} \tag{4.15}$$

The following explicit parameterization for the dielectric function $\epsilon(x)$ is then chosen to be:

$$\epsilon(x) = \epsilon_2 + (\epsilon_1 - \epsilon_2)\Big(\Theta(x - x_0) - \Theta(x - (x_0 + d))\Big)$$

which describes the material distribution (ϵ_1 for the dielectric membrane, ϵ_2 for air) of the two sides of the drum membrane positioned at x_0 (compare Fig. 4.7). Noting that the derivative of the step-function $\Theta(x)$ is the well known Dirac-Delta function $\delta(x)$, the frequency-pull $G^{(1)}$ then reads:

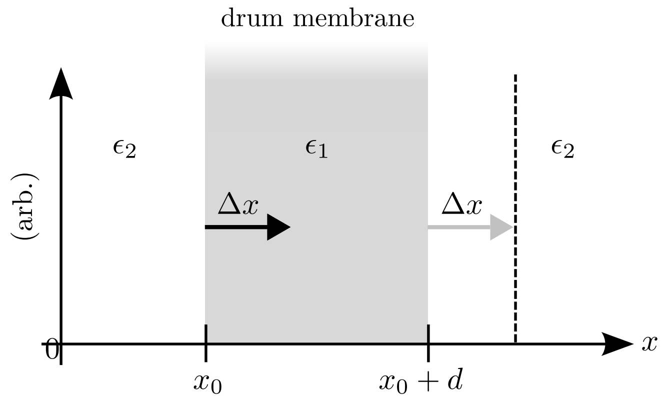

Figure 4.7: Dielectric function $\epsilon(x)$ describing the dielectric permittivity distribution of the drum geometry. The drum membrane (ϵ_1) with thickness d is shifted by a small Δx in positive (x>0) direction towards the surrounding air (ϵ_2).

$$G^{(1)} = \frac{d\omega_{\text{cav}}}{dx} = \frac{\omega_{\text{cav}}^{(0)}}{2} \frac{\int_{S_R} dS \left(1 - \frac{d(x_0+d)}{dx}\right) \Delta\epsilon \left|\mathbf{E}_{\parallel}{}^{(0)}\right|^2 - \int_{S_L} dS \left(1 - \frac{dx_0}{dx}\right) \Delta\epsilon \left|\mathbf{E}_{\parallel}{}^{(0)}\right|^2}{\int_V dV \epsilon(x) \left|\boldsymbol{E}_{\parallel}^{(0)}\right|^2} \tag{4.16}$$

where S_R (S_L) is the surface area on the right (left) side of the drum membrane (that overlaps with the optical mode) with the total resonator volume V and $\Delta\epsilon = \epsilon_1 - \epsilon_2$. Furthermore, only the parallel component (w.r.t the membrane interface) of the electric field has been considered, while the orthogonal component is neglected for the plane-wave ansatz [9]. Since the perturbation of the system is assumed to be simply given by a shift of the membrane (with no further deformations of the geometry), the additional derivative terms such as $\frac{d(x_0+d)}{dx}$ can also be neglected. With this, the frequency-pull parameter $G^{(1)}$ can be completely determined by making use of the results from section 4.1.3, more specifically the explicit field distribution of the MIM cavity field from Eq. (4.10).

Even though method 2 delivers virtually identical results to method 1, further insight about the coupling can be gained from the analytic form of Eq. (4.16): For a cavity field with equal field distribution on both sides of the membrane (symmetric case), the numerator will just cancel out and the coupling will always be zero. On the other hand, for the situation where the field on one side of the membrane is maximal whereas on the other side minimal (anti-symmetric case), the frequency-pull factor $G^{(1)}$ and hence the coupling strength g_0 is maximized. An intuitive explanation for this can be gained by thinking about the radiation pressure of the cavity field onto the membrane: for a totally symmetric field distribution on both sides of the membrane, the resulting radiation pressure would just cancel out, not affecting the membrane at all. Vice versa, the totally anti-symmetric case would induce the maximum radiation pressure onto the membrane, resulting in maximum coupling between the optical cavity and mechanical resonator mode. Explicit plots of the cavity field distribution for specific geometries compared to the coupling map are depicted in Fig. 4.8.

[9] If there would be a normal component of the E-field that can not be neglected, the integrals in Eq. (4.15) would not be manifestly defined (due to the discontinuity of the normal component) and the dielectric function would have to be "smoothed out" accordingly [45]

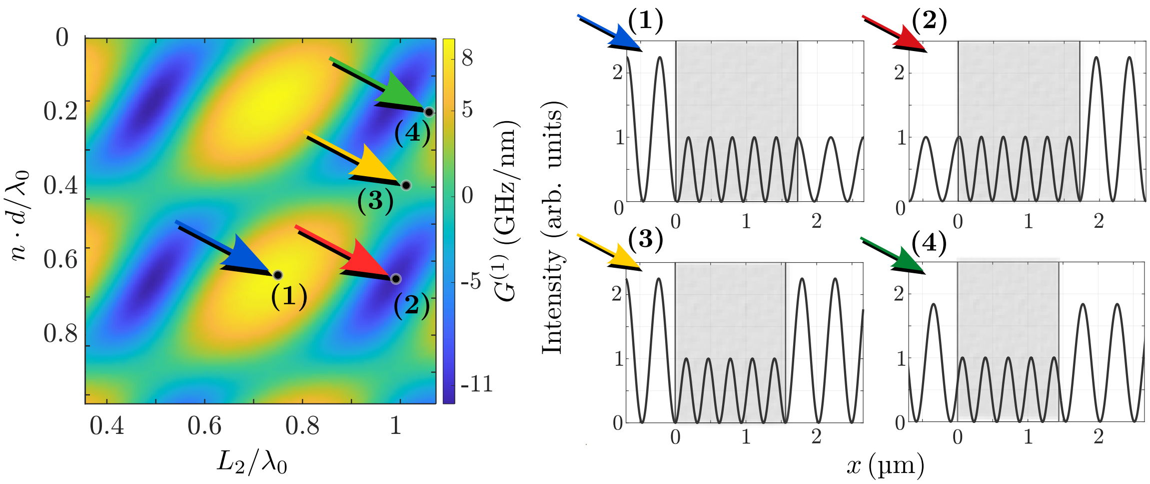

(a) (b)

Figure 4.8: **(a)** Cutout of the linear coupling map from Fig. 4.6 (a). Four points of interest are emphasized. **(b)** Cavity intensity distribution of the four highlighted points from (a). The grayed-out area represents the drum membrane. Each point represents a unique scenario of the field distribution that leads to a given coupling strength: maximum (positive) coupling strength (blue), maximum (negative) coupling strength (red) and zero coupling strength (yellow and green). Case (3) represents the special situation where the drum membrane thickness is exactly equal to a multiple of half the material wavelength and is therefore always zero for any L_2.

4.2 Frequency discrimination and stabilization of a MIM cavity

The overarching goal of this thesis is to measure the coupling strength g_0 of the optomechanical interaction in a MIM-cavity with 3D-laser written polymer membranes. Since it is difficult to directly infer information about the mechanical drum membrane, the only other degree of freedom left is to use the optical field to somehow make this interaction visible. By making use of the standard Pound–Drever–Hall (PDH) frequency stabilization scheme [46] that utilizes a (PHD) error signal to "lock" the system on the cavity resonance frequency, this is made possible.
Since the mechanical resonator is connected to a thermal bath due to the finite temperature of the experiment environment (i.e the lab) there will always be some thermal occupation of the mechanical vibration modes. The drum membrane motion will therefore introduce a very small shift on the resonance frequency ω_{cav} of the optical mode, inducing optomechanical coupling. This will make itself noticeable in the optical mode (i.e the reflection signal that is measured) as a (mechanical) phase-noise contribution that will be overlapped with the reflection signal. Since this noise is exceedingly small compared to other external noise sources of the experiment, a very sensitive measurement scheme has to be utilized to separate out this specific contribution of interest. For this matter, an overview of the employed measurement system is given, followed by a brief overview of the theoretical considerations and practical application of the locking scheme in the context of measuring the mechanical frequency noise.

4.2.1 Experimental setup for cavity frequency locking

The setup used for the PDH stabilization scheme is depicted in Fig. 4.9 (a). It consists of three main components: the MIM-cavity (colored in green), the laser & optics (colored in red, essentially an updated version of the setup introduced in section 2.4) and finally the electronics needed to create the error signal (colored in blue).

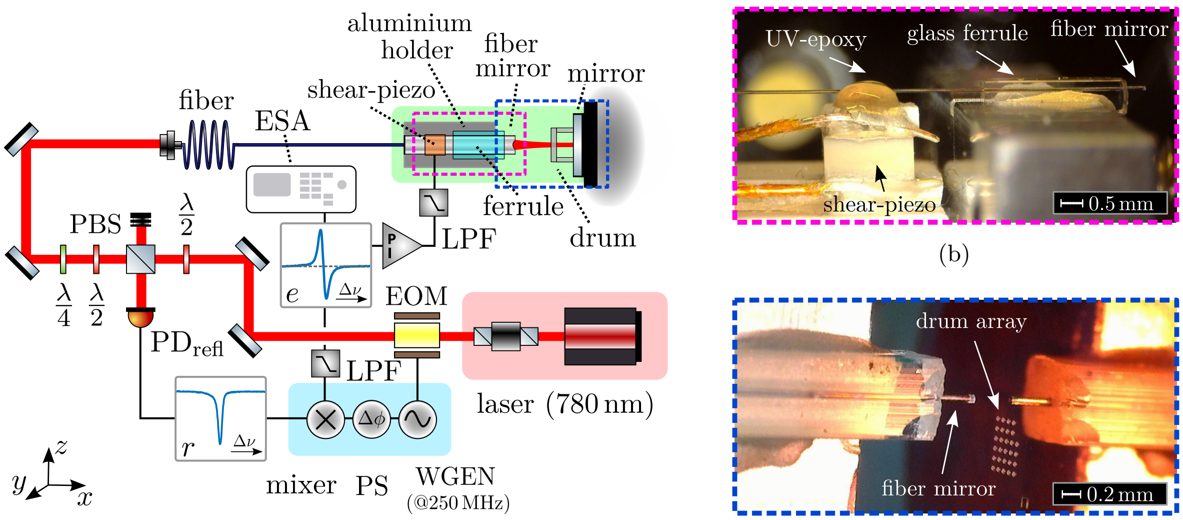

(a) (c)

Figure 4.9: **(a)** The complete experimental setup used for measuring the frequency noise induced by the drum with the PDH technique. It is divided into three main segments: the laser & optics (colored in red) featuring an Electro-Optical-Modulator (EOM), Polarizing-Beam-Splitter (PBS) and photodiode that measures the reflected power of the cavity (PD_{refl}) as a signal "r" (displayed on an oscilloscope); the MIM cavity (colored in green) split up into the fiber & ferrule region (purple dashed box) and cavity region (dark blue dashed box); the electronics (colored in blue) featuring a mixer, phase-shifter (PS) and function generator (WGEN) for the EOM. The error signal "e" (displayed on an oscilloscope) passes a Low-Pass-Filter (LPF) on its way through the Proportional-Integral (PI) feedback controller and is also sent to the Electrical-Spectrum-Analyzer (ESA). An additional LPF is installed after the controller output to clean up the driving signal sent to the shear-piezo. **(b)** Microscope image of the fiber & ferrule region (purple dashed box): the fiber mirror is threaded through a commercial glass ferrule and is glued to a shear-piezo using UV-epoxy. Electrical contacts are glued onto the shear piezo to perform cavity resonance scans. These components are then glued onto a custom-made aluminum holder for easy integration into the setup. **(c)** Microscope image of the cavity region (dark blue dashed box): The aluminum holder that hosts the fiber & ferrule is opposite to a 0.5 inch flat mirror that hosts the polymer drums and is connected to a motorized y-z-translation stage to shift the drum position relative to the fiber mirror.

Starting with the (red) optics branch, a wavelength-tunable laser [10] set to 780 nm in wavelength is guided through an Electro-Optical-Modulator (EOM), essentially a Mach-Zehnder type interferometer used to modulate the phase (or amplitude) of the input beam. The laser beam passes a Polarizing-Beam-Splitter (PBS) with appropriately tuned wave plates before and after the PBS to ensure that any light traveling in the opposite direction (w.r.t the original laser beam path) experiences a 90° shift in polarization and will be caught in the

[10] Lion Series: TEC-500-0770-040

beam path towards the photodiode. After passing the PBS, the laser light is then coupled through a free-space fiber coupler into the opposite end facet of the single-mode fiber-mirror[11] used to build the cavity. As the laser light is coupled into the fiber-mirror, it reaches the cavity branch (colored in green) that is defined by the in-coupling fiber-mirror and the opposing flat mirror on which drum membrane structures have been printed (compare Fig. 4.9 (c)), forming the MIM-system. The flat mirror is installed onto a motorized y-z-translation stage to shift the polymer drum position relative to the fiber mirror. As depicted in Fig. 4.9 (b), the fiber-mirror end of the single-mode fiber is threaded through a glass ferrule [12] to hold the fiber in place. Some portion of the fiber is then glued to a commercial shear-piezo ceramic [13] using a viscous UV-epoxy [14].
By applying voltage to the shear-piezo, the position of the fiber along the x-direction, and by extension the overall cavity size, is shifted. Applying an (amplified [15]) driving triangular voltage signal [16] to the piezo allows to scan the cavity resonances (see Fig. 4.9 (a), denoted by "r").
Finally, additional electronics (colored in blue) are used to create the wanted cavity error signal with a simple dispersive frequency response (denoted by "e" in Fig. 4.9 (a)). After generating the error signal, a Proportional-Integral (PI) feedback loop is used to lock the cavity at the desired frequency. After successfully locking the cavity, the resulting noise signal is then sent to an Electrical-Spectrum-Analyzer (ESA), which essentially decomposes the signal into its frequency components that are then used to measure the optomechanical coupling strength, as will be explained in the following sections.

4.2.2 The Pound-Drever-Hall locking scheme

To explain how the error signal used for locking the cavity is generated, a short introduction to the Pound-Drever-Hall (PDH) locking scheme is given. The practical implementation of this technique for this setup follows in the next paragraph. For further details, standard literature (e.g [47] or [46]) can be consulted.

Theory of the Pound-Drever-Hall scheme Following the laser path from its origin, the laser light first passes through an EOM which modulates the phase of the input laser beam according to the modulation frequency Ω_{mod} from a function generator. The input electric field of the laser is thus modified to:

$$E_{\mathrm{in}} = E_0 \, e^{i(\omega t + \beta \sin(\Omega_{\mathrm{mod}} t))} \tag{4.17}$$

with angular frequency ω, modulation frequency Ω_{mod} and modulation depth β. Expanding Eq. (4.17) by using the Jacobi-Anger expansion (or small angle expansion) to first order [17] leads to:

[11] The single-mode fiber of the fiber mirror is cleaved and fused to a commercial single-mode fiber-patch cable for ease of usage as described in section 2.3

[12] VitroCom: https://www.vitrocom.com/

[13] PI ceramic GmbH: https://www.piceramic.com/

[14] EPO-TEK OG116-31

[15] FLC electronics A800 Voltage Amplifier (100×)

[16] Typical pre-amplified scan amplitudes range from $0.5 - 3\,\mathrm{V}$ peak-to-peak with signal frequencies of around $50 - 100\,\mathrm{Hz}$.

[17] $e^{iz\sin\theta} = \sum_{n=-1}^{1} J_n(z) e^{in\theta}$

$$E_{\text{in}} \approx E_0 \left[J_0(\beta) e^{i\omega t} + J_1(\beta) e^{i(\omega+\Omega_{\text{mod}})t} - J_1(\beta) e^{i(\omega-\Omega_{\text{mod}})t} \right]$$

where J_0, J_1 are the zeroth and first-order Bessel functions of the first kind, respectively. The laser beam now consists of three different beams that are incident on the cavity: the (main) carrier beam with angular frequency ω and two sidebands with modulated frequencies $\omega \pm \Omega_{\text{mod}}$. The resulting reflection signal from the cavity output would now also feature three distinct resonances with the same frequency separation as the incident field. Since the optical linewidths ($\Delta\nu_{\text{FWHM}} > 1\,\text{GHz}$) of our cavities are much larger than the used modulation frequency [18] ($\Omega_{\text{mod}} = 250\,\text{MHz}$), these sideband features can not be resolved here. Nevertheless, the effect of the sidebands that lead to the PDH error signal still remains. The reflected electric field of the cavity can be inferred by multiplying each of the three components by their respective reflection coefficient $R(\omega) = E_r(\omega)/E_{\text{in}}$ (compare Eq. (2.2))[19], which leads to:

$$E_{\text{r}} = E_0 \left[R(\omega)\, J_0(\beta) e^{i\omega t} + R(\omega+\Omega_{\text{mod}})\, J_1(\beta) e^{i(\omega+\Omega_{\text{mod}})t} \; - R(\omega-\Omega_{\text{mod}})\, J_1(\beta) e^{i(\omega-\Omega_{\text{mod}})t} \right]$$

The resulting intensity picked up by photodiode (see Fig. 4.9 (a)) is then just given by $P_{\text{r}} = |E_{\text{r}}|^2$:

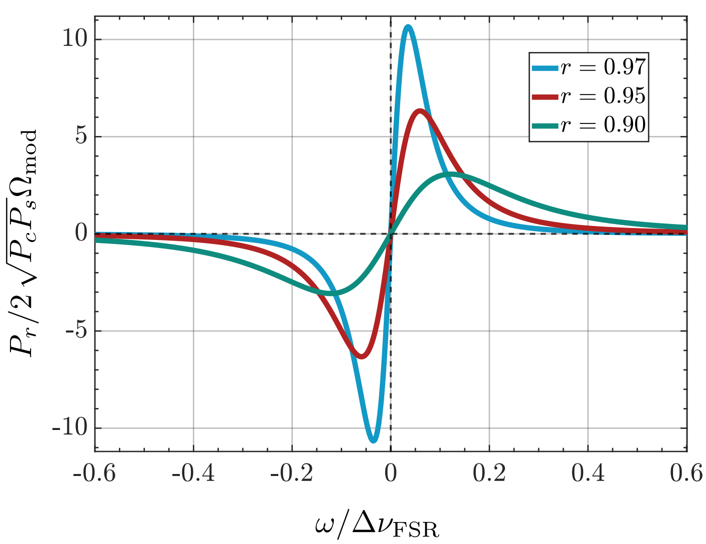

Figure 4.10: Pound-Drever-Hall signal of a symmetric and losses Fabry-Perot cavity ($\Omega_{\text{mod}} < \Delta\nu_{\text{FWHM}}$) for three different reflectivities r. The larger the reflectivity r (or equivalently the Finesse of the cavity), the steeper the error signal becomes.

[18]This approach is just as valid if the modulation frequency Ω_{mod} is above the cavity linewidth $\Delta\nu_{\text{FWHM}}$, here the experiment was just limited by the equipment.

[19]For sake of simplicity, the modification of the reflective coefficient for fiber cavities (from Eq. (2.18)) is neglected. This modification would just introduce a slight asymmetry in the resulting error signal and does not affect the overall behavior.

$$P_{\mathrm{r}} = 2\sqrt{P_c P_s}\left\{\mathrm{Re}\left[\mathcal{R}(\omega,\Omega_{\mathrm{mod}})\right]\cos(\Omega_{\mathrm{mod}}t) + \mathrm{Im}\left[\mathcal{R}(\omega,\Omega_{\mathrm{mod}})\right]\sin(\Omega_{\mathrm{mod}}t)\right\} \\ + (\text{stationary terms}) + (2\,\Omega_{\mathrm{mod}}\text{ terms}). \tag{4.18}$$

with the complex-valued coefficient

$$\mathcal{R}(\omega,\Omega_{\mathrm{mod}}) = R(\omega)R^*(\omega+\Omega_{\mathrm{mod}}) - R^*(\omega)R(\omega-\Omega_{\mathrm{mod}}). \tag{4.19}$$

where $P_c = J_0^2(\beta)\,|E_0|^2$ and $P_s = J_1^2(\beta)\,|E_0|^2$ are the power in the carrier and sidebands, respectively. For slow modulation frequencies ($\Omega_{\mathrm{mod}} < \Delta\nu_{\mathrm{FWHM}}$) as is the case for this setup, Eq. (4.19) can be approximated to:

$$\mathcal{R}(\omega,\Omega_{\mathrm{mod}}) \approx 2\,\mathrm{Re}\left\{R(\omega)\frac{d}{d\omega}R^*(\omega)\right\}\Omega_{\mathrm{mod}} = \frac{d|R|^2}{d\omega}\Omega_{\mathrm{mod}},$$

a purely real-valued quantity. With this, Eq. (4.18) is now just proportional to $\cos(\Omega_{\mathrm{mod}}t)$. Combining this signal with the modulation signal $\sin(\Omega_{\mathrm{mod}}t)$ of the EOM into the input ports of the mixer [20] (see Fig. 4.9 (a)) and carefully adjusting the phase shifter, the term in Eq. (4.18) that varies with $\cos(\Omega_{\mathrm{mod}}t)$ will partly be transformed into a DC-signal, while the rest of the equation will be left with some time dependency. Inserting a low-pass filter after the mixer then filters out all of the time-dependent terms, which leaves the reflected power as:

$$P_r = 2\sqrt{P_c P_s}\frac{d|R|^2}{d\omega}\Omega_{\mathrm{mod}}.$$

This is precisely the wanted error signal that is shown in Fig. 4.9, which can now be used to lock the MIM-cavity. Fig. 4.10 shows an exemplary plot of this error signal for a symmetric and lossless cavity.

Applying the Pound-Drever-Hall scheme to the experiment The previous paragraph explained how the PDH signal is generated. To now actually perform a lock on the cavity, a feedback loop control scheme has to be implemented that uses the PDH signal as a frequency discrimination reference. A simplified sketch of the control loop that is utilized in the experiment is depicted in Fig. 4.11 (a).

Three different signals constituting the locking scheme can be distinguished: the desired setpoint $r(t)$, the process value $y(t)$ and the control function $u(t)$. Here, the setpoint $r(t) = r_0$ is a preset (constant) voltage on the linear slope of the PDH signal and $y(t)$ is given by the voltage on the linear slope of PDH signal at the setpoint frequency (corresponding to $\omega/\Delta\nu_{\mathrm{FSR}} = 0$ in Fig. 4.11 (b)). With this, any deviations of the signal (due to e.g length or frequency instabilities of the cavity) would change the signal value (i.e voltage) of the PDH signal at the setpoint frequency, effectively creating a time-dependent error $e(t) = y(t) - r_0$ (see Fig. 4.11 (b)). The control function $u(t)$ then takes this error, and (after modifying it with the Proportional (P) and Integral (I) element) sends it back to the cavity-length control unit (i.e the shear-piezo) to counteract this deviation from the setpoint r_0. Since the phase sensitivity of the cavity resonance is maximal at the resonance frequency (i.e the minimum point on the reflection signal), it is preferable to lock the cavity at this point to be most sensitive to

[20] A mixer outputs the product of two electrical signal inputs.

the phase noise induced by the polymer drum motion. However, the cavity reflection signal itself can not be utilized for this purpose as it is symmetric around resonance. It is therefore impossible to discriminate if the cavity length (or frequency) must be increased or decreased to compensate a given cavity length (or frequency) drift from the reflection signal alone. Instead, the (anti-symmetric) linear part of the PDH signal needs to be utilized.
Mathematically, the control function $u(t)$ is defined as:

$$u(t) = K_{\mathrm{p}} e(t) + K_{\mathrm{i}} \int_0^t e(\tau) \mathrm{d}\tau$$

with error signal $e(t)$ and the gain parameters K_{p} and K_{i} that are adjusted for the specific lock required. The proportional response takes account of any changes of the error in the moment, while the integral element compensates for any past trends by integrating the error over time.

In principle, this feedback loop would then go on forever and allow the cavity to continuously operate at this one fixed frequency given by the setpoint r_0. In reality, however, the efficiency of the feedback loop is limited by mainly two factors: The overall magnitude and frequency of the instabilities present in the cavity. If the magnitude of the noise onto the cavity shifts the linear part of the PDH signal beyond the setpoint frequency, locking the cavity becomes impossible. Furthermore, the length control unit (i.e the shear-piezo) and the P-I controller itself have an upper-frequency limit at which they can effectively compensate instabilities. It is given by the locking-bandwidth ν_{LB}: The steeper the slope of the linear response of the PDH signal, the larger the resulting error-signal response for a given perturbation of the PDH signal, increasing the sensitivity and compensation speed of the lock [21].

Any noise with frequency beyond this limit cannot be compensated. If these contributions are then of large enough magnitude, locking the cavity again becomes impossible. To that end, the following measures are taken to further stabilize the cavity system and make the locking possible:

- Sorbothane isolation chunks [22] are inserted in-between the aluminum holder that hosts the fiber-mirror and the kinetic mount that hosts the flat mirror to dampen out any low-frequency axial motion between the two sides of the cavity.

- Commercial pyramid foam is used to acoustically isolate the cavity region and also protect against air currents hitting the fiber mirror.

- The weight load on the piezo-electric has also been reduced as far as possible. Before, a commercial piezo-translation stage [23] was used for locking setup. Due to the additional bulk of the translation stage, the system was too slow to compensate high-frequency noises and locking was impossible. After switching to a more miniaturized system (compare Fig. (4.9) (b)), the locking- bandwidth was drastically increased and locking the cavity became possible.

[21] The locking-bandwidth ν_{LB} can be increased by e.g increasing the Finesse of the cavity, increasing the coupling depth of the cavity or in general applying some gain to the reflection signal beforehand.

[22] Thorlabs Inc.: https://www.thorlabs.com/

[23] Thorlabs Inc. NFL5DP20/M

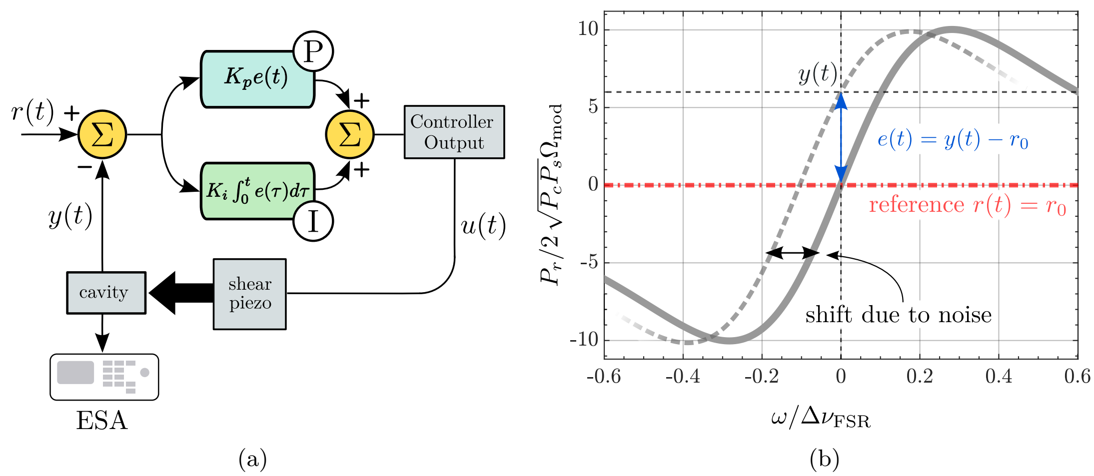

Figure 4.11: (**a**) Block diagram of the P-I controller connected to the cavity. The controller output function $u(t)$ is constantly sent back to the shear-piezo to compensate a frequency shift quantified by the error function $e(t)$=$y(t) - r_0$ by adjusting the cavity length. The resulting signal of the cavity is extracted by an ESA. (**b**) The PDH signal used for the cavity locking with the PI controller. A shift of the PDH signal due to some noise on the cavity resonance induces a frequency shift of the signal (dashed line). The resulting error function $e(t)$ is used to re-stabilize the cavity resonance back to the original reference position.

With this, the cavity can now be successfully locked. The resulting signal $y(t)$ is continuously sent back into the P-I-controller but also forwarded to the ESA, which decomposes the signal into its individual frequency components and displays the magnitude of the noise contributions against its frequency (more formally called Power-Spectral-Density (PSD)). This signal now contains all the noise contributions on the cavity resonance that could not be compensated by the lock, meaning noise frequencies exceeding the locking bandwidth ν_{LB}. Since the simulated eigenfrequency (see chapter 3.2) of the fundamental drum mode ($> 300\,\mathrm{kHz}$) is well above the maximum locking bandwidth of the P-I controller ($\sim 100\,\mathrm{kHz}$), the mechanical resonance can now be very effectively filtered out and examined.

4.3 Measuring the linear optomechanical coupling strength

The extracted PSD obtained after locking the cavity now contains the contributions of the mechanical frequency noise of the drum onto the cavity signal. Here, the noise on the drum position is generated by exchange with the thermal bath of the environment: a (random) thermal force F_{therm} (from the environment) pushing against the harmonic oscillator. To extract the optomechanical coupling strength g_0, a model that describes the PSD frequency noise spectrum measured on the ESA is needed. To that end, a brief sketch of the derivation for the wanted PSD is introduced. Using these results, the optomechanical coupling strength is extracted from the drum noise.

4.3.1 Thermal response of a harmonic oscillator

To start, it is quite useful to introduce the well-known Wiener-Khinchin Theorem [48]:

$$\mathcal{S}_{XX}(\omega) = \int_{-\infty}^{+\infty} d\tau\, e^{-i\omega\tau} \left\langle X(0)X(\tau)\right\rangle \tag{4.20}$$

which connects the (double-sided) PSD $\mathcal{S}_{XX}(\omega)$ with the autocorrelation function $\langle X(0)X(t)\rangle$ as a Fourier-transform. Here, $X(t)$ can be understood as a generic signal or measurand (like the position of a harmonic oscillator). Said autocorrelation function is formally defined as:

$$\left\langle X(t_1)X(t_2)\right\rangle \overset{\Delta t = t_2 - t_1}{=} \lim_{T\to\infty} \frac{1}{T}\int_{-T/2}^{T/2} X(t)^* X(t+\Delta t)dt$$

which, as the name suggests, quantifies the (self) correlation of a (stationary [49]) quantity or signal and only depends on the time difference Δt. To now find the specific PSD corresponding to the motion (x-position) of the harmonic oscillator (drum), the frequency-space solution of the damped forced harmonic ($m_{\text{eff}}\ddot{x} + m_{\text{eff}}\Gamma_m\dot{x} + m_{\text{eff}}\Omega_m^2 x = F_{\text{ext}}$) with the effective mass m_{eff} and damping rate Γ_m can be employed and reads:

$$x(\omega) = \chi_m(\omega)\cdot F_{\text{ext}}(\omega) \tag{4.21}$$

with the susceptibility $\chi_m(\omega)$:

$$\chi_m(\omega) = \left[m_{\text{eff}}\left(\Omega_m^2 - \omega^2\right) - i m_{\text{eff}}\Gamma_m\omega\right]^{-1}$$

connecting the external force $F_{\text{ext}}(\omega)$ to the coordinate response $x(\omega)$ in dependence on the mechanical frequency ω. To now determine $\mathcal{S}_{xx}(\omega)$, one could either directly plug in the expressions for $x(t)$ given by the dampened forced harmonic oscillator into Eq. (4.20), or as a more intuitive argument, use Eq. (4.21) to directly connect the PSD of the x-position of the harmonic oscillator with the thermal force F_{therm}. Here, the latter approach will be used. In analogue to Eq. (4.21) and assuming that the thermal force F_{therm} is stationary [49], the PSD for the displacement fluctuations of the harmonic oscillator can be rewritten as (for a more in-depth justification, refer to Appendix A):

$$\mathcal{S}_{xx}(\omega) = \left|\chi(w)\right|^2 \mathcal{S}_{FF}(\omega) = \left|\chi(w)\right|^2 \int_{-\infty}^{+\infty} d\tau\, e^{-i\omega\tau}\left\langle F_{\text{therm}}(0)F_{\text{therm}}(\tau)\right\rangle. \tag{4.22}$$

The autocorrelation function $\langle F_{\text{therm}}(t_1)F_{\text{therm}}(t_2)\rangle$ of the white thermal force F_{therm} is given by (refer to Appendix B for details):

$$\left\langle F_{\text{therm}}(0)F_{\text{therm}}(t)\right\rangle = 2\Gamma_m k_B T\cdot\delta(t). \tag{4.23}$$

with the Dirac-Delta function $\delta(t)$, Boltzmann-constant k_B and environment temperature T (room temperature $T \approx 20\,°\mathrm{C}$). Plugging Eq. (4.23) back into Eq. (4.22), ones finds:

$$\begin{aligned}\mathcal{S}_{xx}(\omega) = \left|\chi(w)\right|^2 \int_{-\infty}^{+\infty} d\tau\, e^{-i\omega\tau}\left\langle F_{\text{therm}}(0)F_{\text{therm}}(\tau)\right\rangle &= \left|\chi(w)\right|^2 \int_{-\infty}^{+\infty} d\tau\, e^{-i\omega\tau} 2\,\Gamma_m k_B T\cdot\delta(\tau)\\ &= \frac{1}{m_{\text{eff}}}\frac{2\Gamma_{\text{m}}k_{\text{B}}T}{\left(\omega^2-\Omega_{\text{m}}^2\right)^2+\Gamma_{\text{m}}^2\omega^2}\end{aligned}$$

Since the cavity (and the ESA) is not directly sensitive to the noise on the position of the drum membrane, but rather the consequent noise on the resonance frequency, the PSD has to be rewritten one final time (using the frequency-pull parameter $G^{(1)}$), where the single-sided [24] frequency-noise PSD $\mathcal{S}_{\nu\nu}(f)$ reads [36]:

$$\mathcal{S}_{\nu\nu}(f) = 2 \cdot \frac{S_{\omega_{\mathrm{cav}}\omega_{\mathrm{cav}}}(\omega)}{4\pi^2} = 2 \cdot {G^{(1)}}^2 \cdot \frac{S_{xx}(\omega)}{4\pi^2} = \frac{2g_0^2}{4\pi^2} \cdot \frac{2\Omega_m}{\hbar} \cdot \frac{2\Gamma_{\mathrm{m}} k_{\mathrm{B}} T}{\left(\omega^2 - \Omega_{\mathrm{m}}^2\right)^2 + \Gamma_{\mathrm{m}}^2 \omega^2}. \tag{4.24}$$

with the noise frequency $f = \omega/2\pi$ [50]. Eq. (4.24) now finally describes the signal that will be measured by the ESA (after performing frequency calibration on the ESA spectrum). By now locking the MIM cavity on resonance, extracting the PSD with the help of the ESA and using Eq. (4.24), it is now possible to extract the optomechanical coupling strength of the cavity-drum interaction.

4.3.2 Extracted frequency noise spectra of MIM cavities

To now measure the optomechanical coupling strength between the optical cavity and the mechanical drum mode, the MIM system is set up as follows: a flat mirror hosting a drum array consisting of approximately 30 drums with different membrane thickness d and leg height L_2 (see Tab. 4.1) is positioned opposite to the fiber-mirror (compare Fig. 4.9 (c)) to build a cavity of roughly 30 µm in size. Beforehand, the flat mirror orientation is adjusted to yield the largest coupling depth. With this, the flat mirror is facing the fiber-mirror such that the intra-cavity mode is only overlapping with the inner membrane of one of the drums at a time. By now locking the cavity as elaborated in section 4.2.2, the spectrum of the ESA is extracted and examined for resonances that could correspond to the mechanical drum motion.
Since the finite element simulations (section 3.2) predict drum eigenfrequencies in the hundreds of kilohertz, the low-frequency region of the complete scan range of 150 MHz of the ESA is inspected. To make sure that a promising resonance in the ESA spectrum truly corresponds to the noise-induced on the cavity by the drum motion, the same measurement is repeated without a drum membrane between the two mirrors. This rules out that the resonance in question originates from an external noise that doesn't correspond to the drum motion.
An exemplary measurement of the PSD of the frequency noise induced by the thermal motion of the drum membrane is depicted in Fig. 4.12 and displays a resonance that clearly shows the coupling between the cavity mode and the (fundamental) mechanical mode of the laser written polymer drum. Further mechanical resonances corresponding to higher-order drum modes with higher eigenfrequencies have not been found yet and may become visible when the setup is inserted into vacuum (see 4.4).
Since the ESA does not strictly measure the PSD, but rather the spectral power P_{ESA} in dBm, the measurements have to be calibrated to obtain the wanted form of the PSD corresponding to Eq. (4.24). To that end, P_{ESA} is converted into frequency (squared) and finally normalized by the resolution bandwidth $\Delta\nu_{\mathrm{RBW}}$ of the ESA which is chosen to be 9.1 kHz. The conversion from power to frequency (squared) is done by measuring the slope of the linear part of the PDH signal [25] in units of Hz/V.

[24] The ESA is not sensitive to the negative frequencies of a double-sided noise spectrum, and the single-sided PSD is just given by twice the double-sided one.

[25] In the experiment, the PDH signal is displayed as voltage V vs. time t on the oscilloscope. To convert the time axis into frequency, the FSR of the cavity is used for calibration. Since $P \sim V^2$, the slope of the linear

Q_m	$g_0/2\pi$	Ω_m	$\Gamma_m/2\pi$	$\kappa/2\pi$	L_2	d
106 ± 1	$14 \pm 2\,\mathrm{kHz}$	$1.6 \pm 0.1\,\mathrm{MHz}$	$101 \pm 2\,\mathrm{kHz}$	$1 - 3\,\mathrm{GHz}$	$8.3\,\mu\mathrm{m} - 8.7\,\mu\mathrm{m}$	$1.2\,\mu\mathrm{m} - 1.5\,\mu\mathrm{m}$

Table 4.1: "Best-in-class" parameters out of roughly 30 measured drums with differing geometries. The resonance frequencies Ω_m out of the roughly 30 drums were all very close to 1.6 MHz. The rather large error on the coupling strength g_0 is due to the low Finesse of the MIM-system for this specific drum geometry.

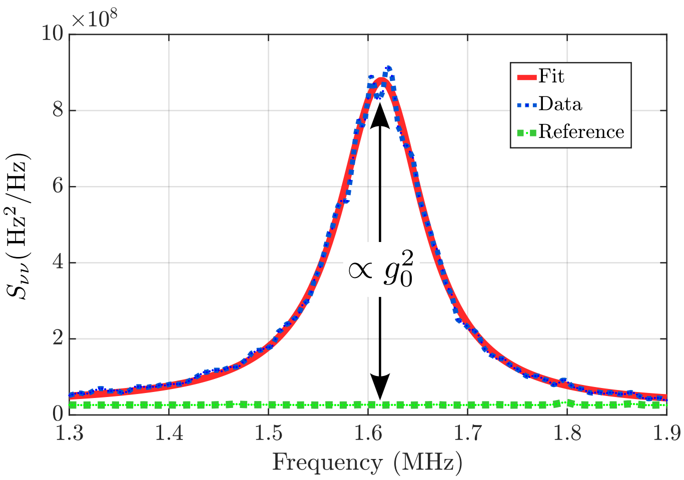

Figure 4.12: The power spectral density $S_{\nu\nu}$ displayed against the mechanical frequency. The data points (blue) are fitted using Eq. (4.24) (red). A reference measurement without the polymer drum is shown in green. The coupling strength can be extracted from the fit and is proportional to the amplitude of the resonance.

With this, the ESA spectrum now properly describes the physics given by Eq. (4.24) with the same units of $\mathrm{Hz}^2/\mathrm{Hz}$. From fitting Eq. (4.24) to the measured spectrum from the ESA, the relevant quantities describing the mechanical drum properties can be extracted. This is done for all of the 30 drums with differing geometries that correspond to different coupling strength scenarios given by the coupling map from Fig. 4.6. The "best-in-class" parameters of the 30 different drum realizations are displayed in Tab. 4.1, including the mechanical quality factor Q_m, the optomechanical coupling strength g_0[26], the mechanical resonance frequency Ω_m, the mechanical dampening rate Γ_m and the corresponding range for typical cavity loss rates $\kappa/2\pi$. Tab. 4.1 also shows that the actually measured parameters differ from the simulated ones from section 3.2: The results for Q_m and Γ_m deviate from the simulations since the measurements are not performed in vacuum (as is assumed in the simulations) but rather in the regular lab environment. Improving these quantities by moving the setup into vacuum is one of the next goals for this experiment, as explained in the following section 4.4.

The deviation of the expected resonance frequency compared to the simulations is most likely due to a lack of knowledge about the actual mechanical material properties of the photoresist used for the DLW and the general uncertainty on the true drum geometry sizes

part of the PDH signal needs to be squared to convert the power spectrum.

[26]Large coupling strengths also typically entail large scattering losses in the MIM system as the field intensity has to be maximized at the polymer surface. This reduces the slope of the PDH signal and the corresponding sensitivity of the measurement and results in a rather large error for large coupling strengths.

(compare section 3.2). Since the values for L_2 and d shown in Tab. 4.1 are just the desired input into the *NanoScribe* system, it is unclear how close these inputs are to the real quantities after the printing process (with potential deviations of up to a 1 µm). For that reason, a calibration of the drum geometry will also be performed in the near future with the help of an interference microscope [25]. If the size calibration is successful and the actual dimensions of the drum geometry are well understood, these measurements will help to draw further conclusions on the still unknown mechanical properties of the polymer drums.

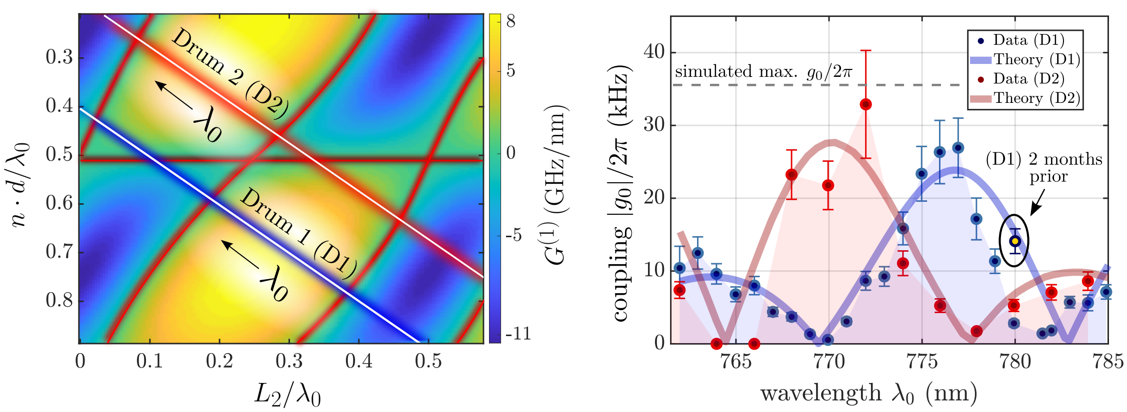

(a) (b)

Figure 4.13: **(a)** Coupling map displaying the linear frequency-pull parameter $G^{(1)}$ against the drum geometry dimensions d and L_2. The zero coupling points are highlighted in dark red. Two diagonal intersections corresponding to the wavelength scan for two polymer drums with different dimensions are displayed: Drum 1 (D1) in blue and Drum 2 (D2) in red. **(b)** Absolute magnitude of the coupling strength $g_0/2\pi$ against the wavelength λ_0 for the two drums. The corresponding theory curves from (a) are overlapped with the measured data points. The simulated maximum coupling is calculated to be at 35 kHz. A measurement of the coupling strength of drum 1 two months prior is highlighted by a black outline.

To now find the largest coupling strength possible for this system, many different drum geometries would need to be measured out to find the one corresponding to a coupling strength maxima (or minima) according to the coupling map in Fig. 4.6. Alternatively, just a single drum can be used by changing the laser wavelength with the help of the tunable wavelength laser. This is essentially equivalent to changing the drum geometry. This is also the reason why the leg height of the drum geometry was chosen to be $L_2 > 8\,\mu\text{m}$, as a scan in the wavelength of $\Delta\lambda_0 = 20 - 30\,\text{nm}$ is equivalent to an effective change of the leg height by $\lambda/2$ (the periodicity of the coupling map). The change of wavelength corresponds to a diagonal cut across the coupling map, where different starting geometries correspond to a horizontal or vertical shift of the lines across the map. Two lines corresponding to the two drums that were measured using this technique are displayed in Fig. 4.13 (a). The resulting absolute magnitude of the coupling strength g_0 is shown in Fig. 4.13 (b), where the theory curves from Fig. 4.13 (a) that are overlapped with the measurements correspond to the "by-eye" best fitting diagonal cut across the coupling map and are not directly fitted to the data itself.
This is due to the number of uncertainties concerning the theory and explains the slight deviation of the theory from the data points. As mentioned previously, the true values of

the drum geometry are not yet fully known and the theory also only considered the ideal case of non-dispersive and perfectly conducting mirrors which — in reality — is not the case. Nevertheless, the theory seems to explain the measurements rather well and optomechanical coupling strengths well above 25 kHz can be reached, close to the maximum value of 35 kHz calculated from the simulated effective mass m_{eff} (compare section 3.2) and the maximum frequency-pull parameter $G^{(1)}$ from the coupling map (compare Fig. 4.6).
Fig. 4.13 (b) also shows that the polymer drums seem to be changing size over time: a similar measurement of drum 1 was performed two months prior to the current results and shows that the coupling strength has changed dramatically. This is only explained by a change in the size of the drum (of a few nanometers) and is believed to arise due to a shrinkage of the drum geometry as the photoresist is further drying out over time. Since this might prove problematic in terms of the consistency of the measurements, the extent of this change has to be further analyzed in the future.
To now add context to these measurements, a table comparing this novel MIM cavity to other more established platforms for MIM resonators is listed in Tab. 4.2. It features a collection of MIM systems that all make use of (mostly) commercial silicon nitride (SiN) membranes with high quality mechanical ($Q_m > 10^6$) and optical properties [17] suitable for optomechanical experiments, instead of the DLW polymer drums used in this work. Most of the works feature "macroscopic" cavity optics, while others ([38], [39]) are also using fiber-cavities and therefore offer a better comparison.

Publication	Ω_m	$\Gamma_m/2\pi$	$\kappa/2\pi$	$G^{(1)}$	$g_0/2\pi$
Thompson et al. (2008) [12]	134 kHz	12 Hz	150 kHz	8.4 MHz/nm	300 Hz
Flowers-Jacobs et al. (2012) [38]	1.7 MHz	87 Hz	0.1 GHz	3 GHz/nm	–
Hornig et al. (2020) [51]	7 MHz	35 kHz	37 GHz	25 GHz/nm	6.8 kHz
de Jong et al. (2020) [52]	150 kHz	0.15 Hz	600 kHz	–	2 Hz
Piergentili et al. (2021) [53]	230 kHz	1.6 Hz	33 kHz	–	0.33 Hz
Rochau et al. (2021) [39]	932 kHz	4.7 Hz	16.8 MHz	1 GHz/nm	1 Hz
This thesis (so far)	1.6 MHz	101 kHz	1 GHz	11 GHz/nm	> 25 kHz

Table 4.2: Comparison of the most decisive optomechanical quantities between this experiment and other, more well-established MIM experiments. The values stated for this thesis correspond to the maximum values achieved so far for each category.

While the optomechanical coupling strength of the polymer drum MIM cavity already delivers promising results, the remaining parameters are still mostly subpar. As mentioned, the experiment is not yet performed in vacuum which will drastically increase the mechanical quality of the drum membrane and efforts have been made to further improve the optical quality as well, as touched on in section 3.3.1. The polymer drum MIM cavity also offers major advantages in terms of flexibility and integration into the fiber cavity, as almost any arbitrary dielectric geometry can be written and easily implemented into the system. The shift to a complete FFPC also allows for further miniaturization and is discussed in the following outlook.

4.4 Outlook: FFPC with polymer membranes in vacuum

Up to this point, all measurements of the optomechanical coupling strength were performed in air. Since the motion of the mechanical drum membrane is heavily damped and restricted in such an environment, the next step to take is to perform these measurements in a regulated vacuum chamber. This will drastically increase the mechanical Q-factor and previously unseen mechanical resonances of higher-order drum modes with higher eigenfrequencies may become visible in the frequency noise spectrum [27]. By improving the mechanical Q-factor (and the mechanical linewidth $\Gamma_m/2\pi$), small shifts of the mechanical resonance frequency due to the optical spring effect [13] may be resolved and measured.

The MIM setup utilized so far is still not compact enough (and also features vacuum-incompatible components) to be installed into our vacuum chamber (see Fig. 4.14). To remedy this issue, the compactness and intrinsic vacuum compatibility of the complete FFPC can be utilized. This is achieved by using glass ferrules to compactly integrate fibers into a monolithic cavity setup. Instead of printing the polymer drums onto a flat macroscopic mirror, a fiber-end facet will host just a singular drum structure and combined with the in-coupling fiber-mirror, our MIM cavity can be drastically miniaturized.

This chapter serves as an extended outlook and gives an overview of the vacuum chamber, the fabrication of the monolithic FFPCs and the attempted (and failed) implementation of the FFPCs into the vacuum chamber.

The vacuum chamber The geometry of the vacuum chamber is shown in Fig. 4.14. It features a 30 cm × 15 cm cylindrical main chamber with three outgoing flange branches. Two are used to evacuate the chamber by first doing a gross pumping of the setup with a turbopump [28] to sufficient pressure levels that allow for the operation of the ion pump [29]. Afterwards, the turbopump is turned off, as it introduces large mechanical vibration that may compromise the quality of the measurements, and the ion pump is turned on to keep the pressure at the desired level.

A small "X"-flange that is connected to the main chamber is used as the experimental chamber for the monolithic FFPC (see Fig. 4.14, red dashed rectangle). It features a fiber feedthrough made by drilling a small opening into the flange that is also connected to a pipe fitting. In order to test the overall performance of the chamber, a test-fiber is threaded through the small opening (see Fig. 4.14, blue dashed rectangle) and through a small custom-made perforated Teflon cone that is situated inside the pipe fitting. The screw cap of the pipe fitting is then tightly screwed shut, squeezing the Teflon piece into the pipe fitting to seal the fiber entrance. This offers an easy way to seal the fiber feedthrough without relying on epoxies to permanently and irreversibly seal the fiber entrance. Another port of the X-flange is used as an electrical feedthrough (see Fig. 4.14, green dashed rectangle) to power the piezo that will scan the FFPC, while the final port is left unused as a glass viewport (see Fig. 4.14, orange dashed rectangle). The final pressure levels achieved for this test-run of the chamber (without bake-out) reached up to $P \approx 5 \cdot 10^{-9}$ mbar (read-out from the ion pump sensor), which is more than sufficient for first tests with optomechanical structures inside the vacuum chamber.

[27] Higher-order modes at higher resonance frequencies become interesting for resolved-sideband cooling of the mechanical drum, where energy from the membrane vibration is dumped into cavity field to potentially cool the drum membrane down to its ground state [13].

[28] Leybold Vacuum PT 70

[29] Agilent Technologies Vacion plus 75 Starcell

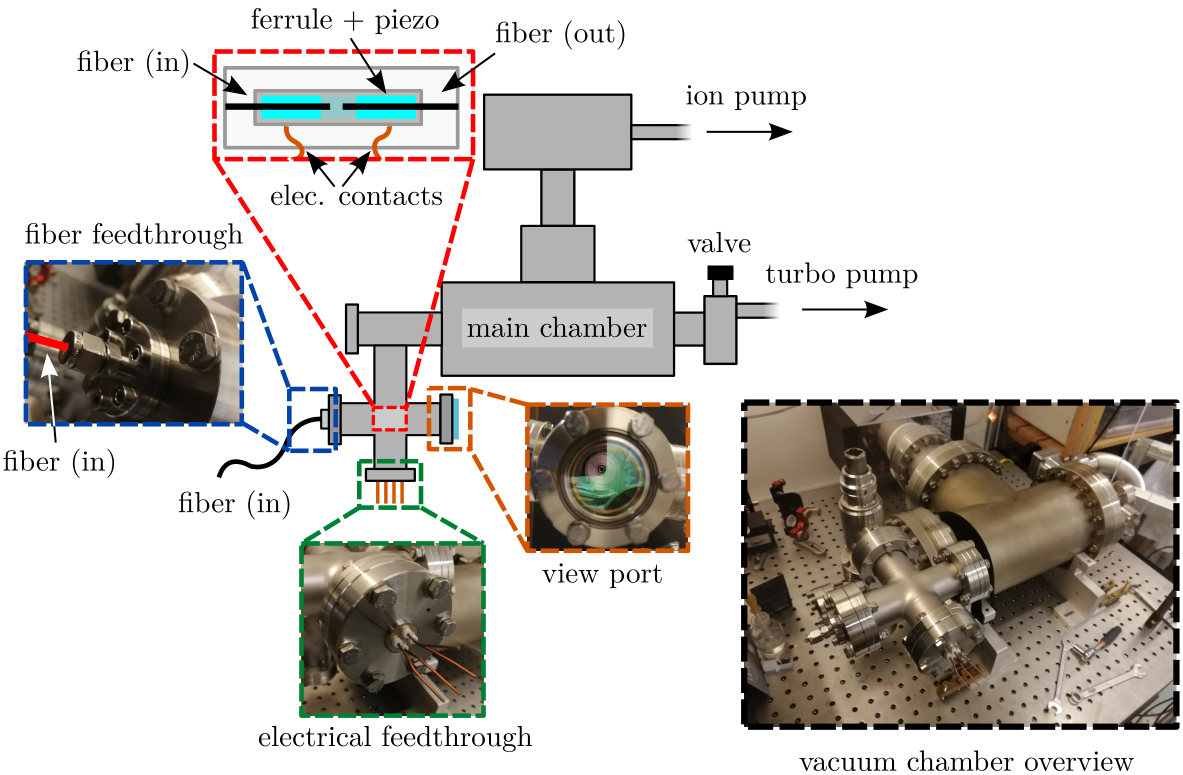

Figure 4.14: Complete vacuum chamber setup. The main chamber is connected to a turbo- and an ion pump used to evacuate the setup. The experiment chamber is connected to the main chamber and will be used to host the monolithic FFPC (marked by the red dashed rectangle) explained in the following paragraph. The in-coupling fiber of the cavity is threaded through a feedthrough inside the flange (marked by the blue dashed rectangle). The out-coupling fiber is not further connected to the outside, as the transmission is not measured for this experiment. For visual clarity, the test-fiber that is threaded through the fiber feedthrough is marked in red. At the front, an electrical feedthrough connects the copper wires connected to the monolithic FFPC to the outside (marked by the green dashed rectangle). Finally, the last flange end is left open as an additional viewport (marked by the orange dashed rectangle). An overview of the full vacuum chamber setup is given in the black dashed inset at the bottom.

Design and fabrication of monolithic FFPCs The centerpiece to the monolithic FFPC is the glass ferrule [30] - a solid 8 mm × 1.25 mm × 1.25 mm large block made of fused silica with a single bore featuring an inner diameter of 131 µm. The bore hosts two opposing fiber mirrors each with a diameter of 125 µm. Thus, the mirror alignment is strictly limited to a relative translation and rotation between fibers (in contrast to the hybrid cavities used in section 4.1.1) and the obtainable Finesse and coupling depth values strongly depend on the quality of the fiber mirror fabrication [50]. Even though this might retrospectively decrease the expected Finesse and coupling depth of the cavity compared to the hybrid system, this monolithic design benefits from high passive stability [50] and vacuum compatibility.
To be able to freely scan the cavity over multiple FSR, the ferrule is glued (using silver epoxy [31]) to a ceramic piezo element [32] of dimensions 10 mm × 2 mm × 1 mm large enough to host

[30] VitroCom: https://www.vitrocom.com/
[31] EPO-TEK H20E-PFC
[32] PI ceramic GmbH: https://www.piceramic.com/

the ferrule.

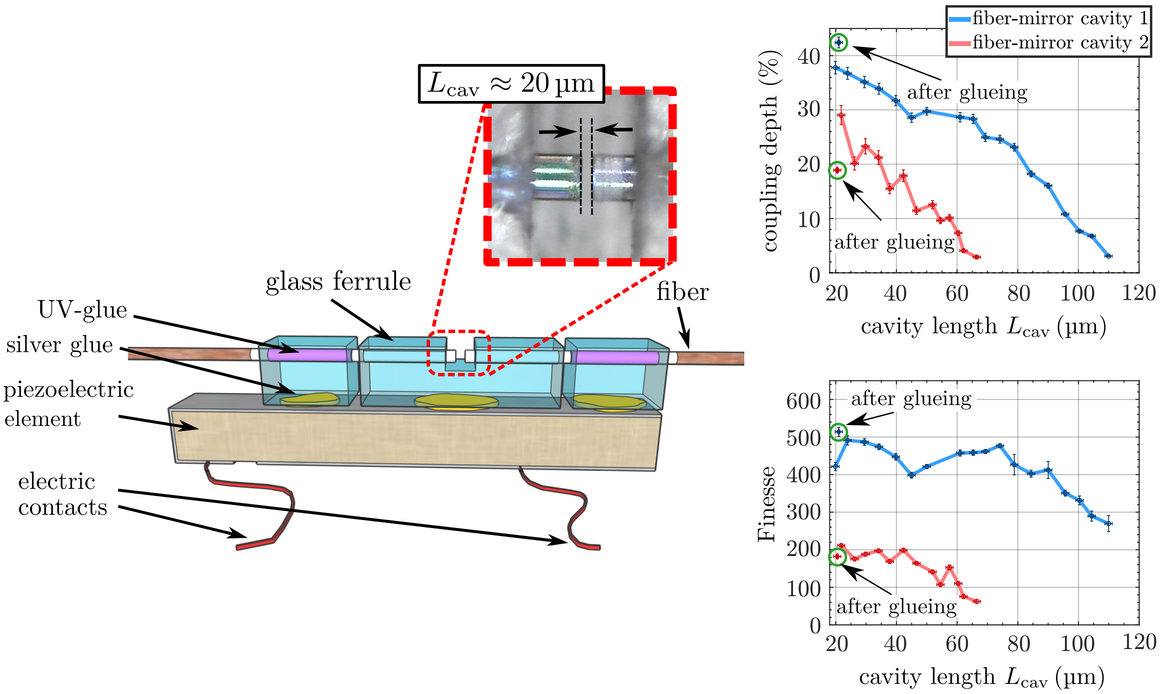

(a) (b)

Figure 4.15: **(a)** Schematic of the monolithic FFPC. The inset in the red dashed box shows a microscope picture of two opposing fiber-mirrors glued inside a glass ferrule. Image adapted from [50]. **(b)** Finesse and coupling depth of two monolithic FFPCs with coated drums against the cavity length L_{cav}. The values after gluing are outlined in green.

Copper wires are fixed to the two contacts of the piezo ceramic with the conductive silver glue. By again applying a triangular signal, the piezo-electric element (and hence the glass ferrule) performs a longitudinal deformation along the fiber axis, which by fixing the two fibers in the glass bore with UV-epoxy [33] [34] allows for scanning the cavity length up to a few FSR [35] (for the ferrules fabricated here, typically $2-3$ FSR were possible). A sketch of the resulting monolithic FFPC is depicted in Fig. 4.15 (a).
As a first test, two monolithic FFPCs were built featuring a $T_1 = 2000\,\mathrm{ppm}$ in-coupling fiber mirror and a bare fiber-end facet hosting a single polymer drum that has been coated with the same reflective coating ($T_2 = 2000\,\mathrm{ppm}$) as the in-coupling fiber [36]. With this, the cavities are now of the generic "mirror-on-a-spring" type. Before gluing the fibers into place, a Finesse and coupling depth analysis is performed to measure the overall optical performance of the specific fiber combinations against different cavity lengths (refer to Fig. 4.15 (b)). The measured Finesse is much lower than the expected $\mathcal{F} \approx 1500$. This is most likely due a to less than ideal

[33] EPO-TEK OG116-31

[34] The UV-epoxy is applied after the fibers are properly aligned inside the ferrule and the final cavity length is fixed. After applying a small droplet of the UV-glue at the entrance of the bore, capillary forces between the fiber and the bore-walls suck in the epoxy which is subsequently hardened by UV-illumination.

[35] The triple slotted ferrules used here allow for larger FSR scan ranges [50]

[36] Since there was no time left to print polymer drums on coated fibers, fiber-end facets with coated polymer drums from an old coating run were used instead.

coating procedure that introduced cracks and irregularities into the mirror coating on the drum since the coating procedure is not yet optimized to include polymer membranes. After evaluating the Finesse measurements, a final cavity length of $L_{\text{cav}} = 20\,\mu\text{m}$ is chosen and the fibers are finally glued in place.

Attempting to measure the optomechanical coupling strength Before finally inserting the FFPCs into the vacuum chamber, a cavity-lock is performed to characterize the mechanical properties of the drum out of vacuum. However, neither cavity displayed a mechanical noise resonance corresponding to the drum motion, even after scanning over the whole frequency spectrum of the ESA (up to roughly 150 MHz). There are a few possible reasons that could explain this behavior: since the fiber-end facets hosting the drum structures were sent out and delivered to the coating company, the fragile drums might have been severely damaged during the delivery (or completely destroyed), hampering the mechanical motion of the membrane. Additionally, the reflective coating on the drum membrane itself might also further damp out the drum motion.
Since both drums did not show any signs of a mechanical resonance out of vacuum, the monolithic drum FFPCs have not yet been inserted into the vacuum chamber. As the next step, un-coated drums will be directly printed onto fibers mirrors again (creating a MIM cavity), without sending them through a coating run. This will reduce the risk of damaging the polymer drums and hopefully allow for a successful implementation of the FFPCs into the vacuum chamber.
Afterwards, it is planned to try to measure the optical spring effect, as it is a standard phenomenon that occurs in optomechanical systems in the unresolved-sideband regime ($\kappa > \Omega_m$). It describes the shift on the mechanical resonance frequency $\delta\Omega_m$ due to the optomechanical interaction [13]:

$$\delta\Omega_m(\Delta)\big|_{\kappa\gg\Omega_m} = g_0^2 \bar{n}_{\text{cav}} \frac{2\Delta}{\kappa^2/4 + \Delta^2} \tag{4.25}$$

with cavity detuning Δ, optical loss rate κ, average cavity photon number $\bar{n}_{\text{cav}}$ and the optomechanical coupling strength g_0. Eq. (4.25) also implies that the drum resonator will be spring softened for red-detuned light ($\Delta < 0$) and spring hardened for blue-detuned light ($\Delta > 0$). In the case of the polymer drum cavity, the expected frequency shifts are approximated to be in the range of a few kilohertz.

Chapter 5

Conclusion and outlook

As a first step towards polymer-based MIM fiber-Fabry-Perot cavities, a hybrid cavity experiment consisting of an in-coupling fiber-mirror and a flat mirror that hosts 3D laser-written membranes has been successfully set up. Optomechanical coupling between the mechanical mode of the membrane and the optical mode of the cavity has been measured with coupling strengths above 25 kHz. As a next step, monolithic FFPCs will be utilized to integrate the MIM system into a vacuum chamber. Further optimizations of the drum geometry are planned to improve the measured mechanical Q_m factor. Moreover, higher-order vibrational modes of the drum (such as the aforementioned breathing modes) with larger mode frequency will be investigated to progress towards a sideband resolved system ($\kappa < \Omega_m$) [13]. This also requires substantial improvements of the optical quality of the polymer membrane. Further rigorous testing of different polishing techniques has to be performed to fully optimize the polymer structures.

After the full characterization and optimization of the single drum MIM experiment, the next step will be the extension of the system towards multiple coupled mechanical resonators. This will allow us to study collective phenomena of mechanical resonators [54], increase the optomechanical coupling to collective mechanical modes [55], and ultimately lead to mechanical metamaterials that can be interfaced through optical cavities [56]. One possible realization of this could be a stack of multiple polymer drums taking advantage of the flexible fabrication offered by the direct laser writing technique.

A possible application of the 3D laser written MIM cavity is that of a highly sensitive force sensor. This has advantages over conventional sensors in terms of an all-optical readout, still offering strong compactness and integrability.

Finally, the presented MIM cavity can also be a potential platform for coupling optical and microwave resonators via an intermediate mechanical mode. This would require to couple the mechanical membrane to a microwave resonator or ideally directly integrate it onto the tip of the optical fiber system. First implementations of electrical contacts on fiber end facets have been realized by the group of Prof. Linden and pave the way to combine the current system with electrical elements. This would have the potential to serve as a platform for unitary frequency conversion for quantum networking.

All in all, fiber cavities with integrated 3D laser-written polymer membranes for optomechanical experiments present a promising platform for tackling the future challenges in cavity optomechanics.

Bibliography

[1] P. Meystre. “A short walk through quantum optomechanics”. In: *Annalen der Physik* 525.3 (2012), 215–233. ISSN: 0003-3804. DOI: 10.1002/andp.201200226.

[2] J. Melcher et al. “A self-calibrating optomechanical force sensor with femtonewton resolution”. In: *Applied Physics Letters* 105.23 (2014), p. 233109. DOI: 10.1063/1.4903801.

[3] R. W. Andrews et al. “Bidirectional and efficient conversion between microwave and optical light”. In: *Nature Physics* 10.4 (2014), 321–326. ISSN: 1745-2481. DOI: 10.1038/nphys2911.

[4] V. Braginsky and A. Manukin. “Ponderomotive Effects of Electromagnetic Radiation”. In: *Soviet Physics Journal of Experimental and Theoretical Physics* (1967).

[5] A. Dorsel et al. “Optical Bistability and Mirror Confinement Induced by Radiation Pressure”. In: *Phys. Rev. Lett.* 51 (17 1983), pp. 1550–1553. DOI: 10.1103/PhysRevLett.51.1550.

[6] B. S. Sheard et al. “Observation and characterization of an optical spring”. In: *Phys. Rev. A* 69 (5 2004), p. 051801. DOI: 10.1103/PhysRevA.69.051801.

[7] T. Corbitt et al. “Optical Dilution and Feedback Cooling of a Gram-Scale Oscillator to 6.9 mK”. In: *Phys. Rev. Lett.* 99 (16 2007), p. 160801. DOI: 10.1103/PhysRevLett.99.160801.

[8] I. Favero et al. “Fluctuating nanomechanical system in a high finesse optical microcavity”. In: *Opt. Express* 17.15 (2009), pp. 12813–12820. DOI: 10.1364/OE.17.012813.

[9] M. Eichenfield et al. “A picogram- and nanometre-scale photonic-crystal optomechanical cavity”. In: *Nature* 459.7246 (2009), 550–555. ISSN: 1476-4687. DOI: 10.1038/nature08061.

[10] X. Jiang et al. “High-Q double-disk microcavities for cavity optomechanics”. In: *Opt. Express* 17.23 (2009), pp. 20911–20919. DOI: 10.1364/OE.17.020911.

[11] F. Brennecke et al. “Cavity Optomechanics with a Bose-Einstein Condensate”. In: *Science* 322.5899 (2008), pp. 235–238. DOI: 10.1126/science.1163218.

[12] J. Thompson et al.
"Strong dispersive coupling of a high-finesse cavity to a micromechanical membrane".
In: *Nature* 452 (2008). DOI: https://doi.org/10.1038/nature06715.

[13] M. Aspelmeyer, T. J. Kippenberg, and F. Marquardt. "Cavity optomechanics".
In: *Rev. Mod. Phys.* 86 (4 2014), pp. 1391–1452. DOI: 10.1103/RevModPhys.86.1391.

[14] C. Saavedra et al. "Tunable fiber Fabry-Perot cavities with high passive stability".
In: *Optics Express* 29.2 (2021), p. 974. ISSN: 1094-4087. DOI: 10.1364/oe.412273.

[15] T. Macha et al. "Nonadiabatic storage of short light pulses in an atom-cavity system".
In: *Physical Review A* 101.5 (2020). ISSN: 2469-9934.
DOI: 10.1103/physreva.101.053406.

[16] D Hunger et al. "A fiber Fabry–Perot cavity with high finesse".
In: *New Journal of Physics* 12.6 (2010), p. 065038.
DOI: 10.1088/1367-2630/12/6/065038.

[17] B. M. Zwickl et al. "High quality mechanical and optical properties of commercial silicon nitride membranes". In: *Applied Physics Letters* 92.10 (2008), p. 103125.
DOI: 10.1063/1.2884191.

[18] D. Meschede. *Optik, Licht und Laser*. Vieweg+Teubner Verlag, 2008.
DOI: 10.1007/978-3-8348-9288-1.

[19] *Laser Resonators and Gaussian Beams*. John Wiley and Sons, Ltd, 2010.
Chap. 7, pp. 269–329. ISBN: 9780470409718.
DOI: https://doi.org/10.1002/9780470409718.ch7.
eprint: https://onlinelibrary.wiley.com/doi/pdf/10.1002/9780470409718.ch7.

[20] F. Pampaloni and J. Enderlein.
"Gaussian, Hermite-Gaussian, and Laguerre-Gaussian beams: A primer".
In: *arXiv: Optics* (2004).

[21] D. Z. Anderson. "Alignment of resonant optical cavities".
In: *Appl. Opt.* 23.17 (1984), pp. 2944–2949. DOI: 10.1364/AO.23.002944.

[22] C. Cohen-Tannoudji, B. Diu, and F. Laloë. *Quantum mechanics; 1st ed.*
Trans. of : Mécanique quantique. Paris : Hermann, 1973. Wiley, 1977.

[23] W. B. Joyce and B. C. DeLoach. "Alignment of Gaussian beams".
In: *Appl. Opt.* 23.23 (1984), pp. 4187–4196. DOI: 10.1364/AO.23.004187.

[24] D. Röser. "Fiber Fabry-Perot Cavities for Quantum Information and Spectroscopy".
2019.

[25] J. C. Gallego.
"Strong Coupling between Small Atomic Ensembles and an Open Fiber Cavity". 2017.

[26] Igor Dotsenko. "Single atoms on demand for cavity QED experiments".
Rheinische Friedrich-Wilhelms-Universität Bonn, 2007.

[27] M. Uphoff et al.
"Frequency splitting of polarization eigenmodes in microscopic Fabry–Perot cavities".
In: *New Journal of Physics* 17.1 (2015), p. 013053. ISSN: 1367-2630.
DOI: 10.1088/1367-2630/17/1/013053.

[28] M. Kubista. "A New Fiber Mirror Production Setup". 2017.

[29] R. Kitamura, L. Pilon, and M. Jonasz. "Optical constants of silica glass from extreme ultraviolet to far infrared at near room temperature". In: *Appl. Opt.* 46.33 (2007), pp. 8118–8133. DOI: 10.1364/AO.46.008118.

[30] X. Zhou, Y. Hou, and J. Lin. "A review on the processing accuracy of two-photon polymerization". In: *AIP Advances* 5.3 (2015), p. 030701. DOI: 10.1063/1.4916886.

[31] F. Brückerhoff-Plückelmann. "Dielectric Waveguide Fabrication by Direct Laser Writing". 2019.

[32] M. Schmid, D. Ludescher, and H. Giessen. "Optical properties of photoresists for femtosecond 3D printing: refractive index, extinction, luminescence-dose dependence, aging, heat treatment and comparison between 1-photon and 2-photon exposure". In: *Opt. Mater. Express* 9.12 (2019), pp. 4564–4577. DOI: 10.1364/OME.9.004564.

[33] M. Göppert-Mayer. "Über Elementarakte mit zwei Quantensprüngen". In: *Annalen der Physik* 401.3 (1931), pp. 273–294. DOI: https://doi.org/10.1002/andp.19314010303. eprint: https://onlinelibrary.wiley.com/doi/pdf/10.1002/andp.19314010303.

[34] T. Frenzel, M. Kadic, and M. Wegener. "Supplementary Material: Three-dimensional mechanical metamaterials with a twist". In: *Science* 358.6366 (2017), pp. 1072–1074. DOI: 10.1126/science.aao4640.

[35] J. Bauer et al. "Thermal post-curing as an efficient strategy to eliminate process parameter sensitivity in the mechanical properties of two-photon polymerized materials". In: *Opt. Express* 28.14 (2020), pp. 20362–20371. DOI: 10.1364/OE.395986.

[36] M. L. Gorodetksy et al. "Determination of the vacuum optomechanical coupling rate using frequency noise calibration". In: *Opt. Express* 18.22 (2010), pp. 23236–23246. DOI: 10.1364/OE.18.023236.

[37] S. Groeblacher et al. "Observation of strong coupling between a micromechanical resonator and an optical cavity field". In: *Nature* 460 (Aug. 2009), pp. 724–7. DOI: 10.1038/nature08171.

[38] N. E. Flowers-Jacobs et al. "Fiber-cavity-based optomechanical device". In: *Applied Physics Letters* 101.22 (2012), p. 221109. DOI: 10.1063/1.4768779.

[39] F. Rochau et al. "Dynamical Backaction in an Ultrahigh-Finesse Fiber-Based Microcavity". In: *Physical Review Applied* 16.1 (2021). ISSN: 2331-7019. DOI: 10.1103/physrevapplied.16.014013.

[40] D. H. Santamore, A. C. Doherty, and M. C. Cross. "Quantum nondemolition measurement of Fock states of mesoscopic mechanical oscillators". In: *Phys. Rev. B* 70 (14 2004), p. 144301. DOI: 10.1103/PhysRevB.70.144301.

[41] M. Aspelmeyer, T. Kippenberg, and F. Marquardt. *Cavity Optomechanics. Nano- and Micromechanical Resonators Interacting with Light.* Springer, 2014. Chap. 1.

[42] D. J. Griffiths. *Introduction to electrodynamics; 4th ed.* Re-published by Cambridge University Press in 2017. Pearson, 2013.

[43] K. Ujihara.
Output Coupling in Optical Cavities and Lasers: A Quantum Theoretical Approach.
Wiley, 2010. Chap. 1.

[44] K. Fujii.
Introduction to the Rotating Wave Approximation (RWA) : Two Coherent Oscillations.
2014. arXiv: 1301.3585 [quant-ph].

[45] S. G. Johnson et al.
"Perturbation theory for Maxwell's equations with shifting material boundaries".
In: *Phys. Rev. E* 65 (6 2002), p. 066611. DOI: 10.1103/PhysRevE.65.066611.

[46] R. W. P. Drever et al.
"Laser phase and frequency stabilization using an optical resonator".
In: *Applied Physics B* 31 (1983), pp. 97–105.

[47] E. D. Black. "An introduction to Pound–Drever–Hall laser frequency stabilization".
In: *American Journal of Physics* 69.1 (2001), pp. 79–87. DOI: 10.1119/1.1286663.

[48] A. A. Clerk et al. "Introduction to quantum noise, measurement, and amplification".
In: *Reviews of Modern Physics* 82.2 (2010), 1155–1208. ISSN: 1539-0756.
DOI: 10.1103/revmodphys.82.1155.

[49] D. T. Gillespie. "The mathematics of Brownian motion and Johnson noise".
In: *American Journal of Physics* 64.3 (1996), pp. 225–240. DOI: 10.1119/1.18210.

[50] C. Saavedra et al. "Supplementary document for Tunable Fiber Fabry-Perot Cavities with High Passive Stability". In: *Opt. Express* 29.2 (2021), pp. 974–982.
DOI: 10.1364/OE.412273.

[51] G. J. Hornig, L. Bu, and R. G. DeCorby.
"Monolithically integrated membrane-in-the-middle cavity optomechanical systems".
In: *OSA Quantum 2.0 Conference*. Optical Society of America, 2020, QW6A.2.
DOI: 10.1364/QUANTUM.2020.QW6A.2.

[52] M. H. J. de Jong et al. *Coherent mechanical noise cancellation and cooperativity competition in optomechanical arrays*. 2020. arXiv: 2012.11733 [physics.optics].

[53] P. Piergentili et al. "Absolute Determination of the Single-Photon Optomechanical Coupling Rate via a Hopf Bifurcation". In: *Physical Review Applied* 15.3 (2021).
ISSN: 2331-7019. DOI: 10.1103/physrevapplied.15.034012.

[54] M. H. J. de Jong et al. *Coherent mechanical noise cancellation and cooperativity competition in optomechanical arrays*. 2020. arXiv: 2012.11733 [physics.optics].

[55] A. Xuereb, C. Genes, and A. Dantan.
"Strong Coupling and Long-Range Collective Interactions in Optomechanical Arrays".
In: *Physical Review Letters* 109.22 (2012). ISSN: 1079-7114.
DOI: 10.1103/physrevlett.109.223601.

[56] H. Ren et al. *Topological phonon transport in an optomechanical system*. 2020.
arXiv: 2009.06174 [cond-mat.mes-hall].

[57] Proakis. *Digital Communications 5th Edition*. McGraw Hill, 2007.

[58] V. Z. Marmarelis. "Nonlinear Dynamic Modeling of Physiological Systems". In: 2004.

[59] D. S. Lemons and A. Gythiel. "Paul Langevin's 1908 paper "On the Theory of Brownian Motion" ["Sur la théorie du mouvement brownien," C. R. Acad. Sci. (Paris) 146, 530–533 (1908)]". In: *American Journal of Physics* 65.11 (1997), pp. 1079–1081. DOI: 10.1119/1.18725.

[60] F. Schwabl. *Statistische Mechanik*. Springer-Lehrbuch. Springer, 2000. ISBN: 9783540671589.

Appendix A

Input-output relation for the power spectral density of the harmonic oscillator

To understand Eq. (4.22), a brief derivation of how one finds the relation between the PSD for a given external Force $F(t)$ (input) and a consequent displacement $x(t)$ (output) of a typical forced and dampened harmonic oscillator is shown. To start, consider the standard inhomogeneous differential equation describing such a system:

$$\ddot{x} + \Gamma \dot{x} + \Omega^2 x = \frac{F(t)}{m}. \tag{A.1}$$

In time domain, the solution of Eq. (A.1) is found by considering its Green's function $\chi(t, \tau)$:

$$x(t) = \int_{-\infty}^{+\infty} d\tau \, \chi(\tau) \, F(t - \tau) \tag{A.2}$$

The corresponding autocorrelation function for $x(t)$ is thus given by:

$$\langle x(t_1) x(t_2) \rangle = \int_{-\infty}^{+\infty} d\alpha \, d\beta \chi(\alpha)^* \chi(\beta) \, \langle F(t_1 - \alpha) F(t_2 - \beta) \rangle$$

where Eq. (A.2) has been utilized. Since both the input and output processes are stationary (i.e the autocorrelation functions will only depend on time differences, not absolute time) [49], the equation can be rewritten as [57]:

$$\langle x(0) x(\Delta t) \rangle = \int_{-\infty}^{+\infty} \int_{-\infty}^{+\infty} d\alpha \, d\beta \chi(\alpha)^* \chi(\beta) \left\langle F(0) F(\Delta t') \right\rangle$$

with the substitutions $\Delta t = t_2 - t_1$ and $\Delta t' = \Delta t + \alpha - \beta$. Making use the of the Wiener-Khinchin theorem (Eq. (4.20)), the corresponding PSD $S_{xx}(\omega)$ is found:

$$\begin{aligned} \mathcal{S}_{xx}(\omega) &= \int_{-\infty}^{+\infty} d(\Delta t) \, e^{-i\omega \Delta t} \, \langle x(0) x(\Delta t) \rangle \\ &= \int_{-\infty}^{+\infty} \int_{-\infty}^{+\infty} \int_{-\infty}^{+\infty} d(\Delta t) d\alpha \, d\beta \, \chi(\alpha)^* \chi(\beta) \left\langle F(0) F(\Delta t') \right\rangle e^{-i\omega \Delta t} \end{aligned}$$

performing the substituiton $\Delta t = \Delta t' - \alpha + \beta$ and defining $\chi(\omega)$ as the Fourier transform of $\chi(t)$ leads to the wanted equation:

$$S_{xx} = |\chi(\omega)|^2 S_{FF}$$

connecting the PSD of the input signal ($F(t)$) with the PSD of output signal ($x(t)$) via the well-known mechanical susceptibility of the harmonic oscillator $\chi(\omega)$.

Appendix B

Autocorrelation function of a white thermal force

Assuming a white[1] thermal force acting on the mechanical oscillator, the autocorrelation functions reads [58]:

$$\langle F_{\text{therm}}(t_1)F_{\text{therm}}(t_2)\rangle = f_0 \cdot \delta(t_1 - t_2) \tag{B.1}$$

for times t_1 and t_2 where f_0 is a yet to be determined value. White thermal forces are completely uncorrelated (hence the $\delta(x)$ function in Eq. (B.1)) with zero mean $\langle F_{\text{therm}}(t)\rangle = 0$ and offer a good approximation to model the effects of the environment on the drum membrane. The differential equation that describes the dynamics of such a harmonic oscillator subject to random fluctuating force $F_{\text{therm}}(t)$ is given by the Langevin equation [59], which reads:

$$m_{\text{eff}}\ddot{x} = -\Gamma\dot{x} + F_{\text{therm}}(t) \tag{B.2}$$

where m_{eff} is the effective mass of the oscillator (drum) and Γ the mechanical damping factor. To determine f_0, the equipartition theorem [60] can be employed. By now calculating the noise of the kinetic energy of the drum ($1/2m_{\text{eff}}\left\langle\dot{x}^2(t)\right\rangle$) with Eq. (B.2) and equating it to $k_bT/2$, f_0 can be determined. To that end, the homogeneous solution of Eq. (B.2) reads;

$$\dot{\tilde{x}}(t) = v_0 \cdot e^{-\frac{\Gamma}{m_{\text{eff}}}t}$$

Continuing with the standard procedure, the particular solution is then given by

$$\dot{x}(t) = \dot{\tilde{x}}(t) \cdot G(t) \tag{B.3}$$

with some time dependent function $G(t)$. After plugging Eq. (B.3) back into Eq. (B.2), determining $G(t)$ and formally integrating, one finds:

$$\dot{x}(t) = v_0 \cdot e^{-\frac{\Gamma}{m_{\text{eff}}}t} + \frac{1}{m_{\text{eff}}}\int_0^t e^{-\frac{\Gamma}{m_{\text{eff}}}(t-t')}F_{\text{therm}}\left(t'\right)dt' \tag{B.4}$$

[1] In this context, white (noise) refers to a completely uncorrelated, random signal with a flat spectral density.

where the L.H.S of Eq. (B.4) constitutes the homogeneous solution (the average evolution) and the R.H.S the particular one (the contribution of the random force to the motion). To now determine the fluctuation (noise) of the kinetic energy, $\left\langle \dot{x}^2(t) \right\rangle$ is given by:

$$\begin{aligned}
\left\langle \dot{x}^2(t) \right\rangle &= v_0^2 \cdot e^{-2\Gamma t/m_{\text{eff}}} + \frac{1}{m_{\text{eff}}^2} \int_0^t \int_0^t \underbrace{\left\langle F_{\text{therm}}\left(t_1\right) F_{\text{therm}}\left(t_2\right) \right\rangle}_{= f_0 \cdot \delta(t_1 - t_2)} e^{-2\Gamma t/m_{\text{eff}}} e^{\Gamma(t_1+t_2)/m_{\text{eff}}} dt_1 dt_2 \\
&= v_0^2 \cdot e^{-2\Gamma t/m_{\text{eff}}} + \frac{f_0}{2\Gamma m_{\text{eff}}} \left(1 - e^{-2\Gamma t/m_{\text{eff}}}\right)
\end{aligned}$$

where Eq. (B.1) has been utilized. Finally, for the equilibrium state ($t \to \infty$) of the drum membrane, the equipartition theorem can be used to find:

$$\lim_{t \to \infty} \left\langle \dot{x}^2(t) \right\rangle = \frac{f_0}{2\Gamma m_{\text{eff}}} = \frac{k_B T}{m_{\text{eff}}}$$

This now leads to the desired result for the autocorrelation function for the thermal force $F_{\text{therm}}(t)$:

$$\langle F_{\text{therm}}(t_1) F_{\text{therm}}(t_2) \rangle = f_0 \cdot \delta(t_1 - t_2) = 2\Gamma k_B T \cdot \delta(t_1 - t_2).$$